POLITECNICO DI TORINO

Master's Degree in Energy and Nuclear Engineering

Master's Degree Thesis

3D transient CFD simulation of an in-vessel loss-of-coolant accident in the EU DEMO WCLL breeding blanket

Supervisors

Dr. Andrea ZAPPATORE

Dr. Antonio FROIO

Candidate

Mauro SPRÒ

July 2023

Abstract

Safety is one of the most important aspect in the design of the EU DEMO fusion reactor, therefore it is fundamental to study the Design-Basis Accidents (DBA) already in its pre-conceptual design phase. The in-vessel Loss Of Coolant Accident (LOCA) is one of the most relevant DBA, since it has the potential to seriously damage the components inside the vacuum vessel. Usually this kind of transients are modeled with system-level codes, which are typically employed to analyze the behavior of the entire system and for this reason are based on a lumped approach. However, they are unable to evaluate localized quantities such as pressure peaks, which cannot be neglected during this kind of accidents, since the failure criteria for fusion reactors are directly related to local quantities. To account also for the local parameters, it is necessary to develop a 3D transient model. In this work, an in-vessel LOCA from a water-cooled breeding blanket has been modeled, considering a rupture area of about $1\,m^2$. The implementation was performed in the commercial CFD code STAR-CCM+. The model simulates the propagation of a pressurized water jet (water in the same thermodynamic conditions as in a pressurized water reactor) in the vacuum chamber, starting from the pipe break. In this way it is possible to analyze the whole evolution of the jet, accounting also for the phase-change phenomena expected at the pipe exit due to the huge difference in pressure between the cooling water and the chamber atmosphere. Being the pressure ratio equal to 1550, supersonic flow conditions are expected, as well as strong shock waves, which may propagate throughout the whole torus and bounce back from a wall to another. For this reason, adopting a static mesh is not the best choice, since a huge number of cells would be required to properly solve the jet evolution, as the whole domain must be finely refined. A better approach is to employ an adaptive mesh refinement (AMR) algorithm which, being capable of adapting the mesh to the jet evolution, allows to reduce a lot the number of cells and, as a consequence, to spare a considerable amount of computational time. The physical models adopted have been benchmarked against a 2D reference problem with similar features before being applied to the more complex 3D EU DEMO-relevant case. The simulation results show that the shock wave impacting on the wall in front of the vessel is not dangerous, as the resulting pressure peak is below the design limit. Also the temperatures reached during the transient are not of concern for the integrity of the materials. In order to compare the average pressure evolution with that computed with a system-level code, the shock wave has been followed until the impact on the other side of the torus, where it could potentially cause the opening of the burst disks and then be reflected back. Finally a comparison with the in-vessel LOCA from a helium cooled blanket is performed,

highlighting the main differences and showing how the water jet is less severe and much slower than the helium one, being affected also by phase change phenomena.

Acknowledgements

First and foremost, I would like to thank my parents for giving me the opportunity to embark on this extraordinary five year journey. Without your sacrifices and your encouragement, none of this would have been possible.

Right after, I would like to thank my brother Stefano, for being the best roommate I could have wished for during these years and for always believing in me, sometimes even more than I did myself. Living with you from day one made me feel like we never left home.

Finally, special thanks go to Dr. Froio and Dr. Zappatore for constantly guiding me throughout this journey and for always being available for any of my requests. I have always admired you as people and as teachers, and during the past year you have spurred me on to do my best and helped me achieve important milestones. It was an honor for me to have had the opportunity to work with you. I will be forever indebted to you.

Table of Contents

List of Tables

List of Figures

Acronyms

D
Deuterium

T
Tritium

TF
Toroidal Field

PF
Poloidal Field

BB
Breeding Blanket

EU DEMO
EUropean DEMOnstration

HCPB
Helium-Cooled Pebble-Beds

WCLL
Water-Cooled Lithium-Lead

VV
Vacuum Vessel

FW
First Wall

ITER

International Thermonuclear Experimental Reactor

DBA

Design Basis Accident

LOCA

Loss-Of-Coolant Accident

PWR

Pressurized Water Reactor

RELAP

Reactor Excursion and Leak Analysis Program

GETTHEM

GEneral Tokamak THErmalhydraulic Model

MELCOR

Methods for Estimation of Leakages and Consequences of Releases

CFD

Computational Fluid Dynamics

IAPWS-IF97

International Association for the Properties of Water and Steam, Industrial Formulation 1997

LES

Large Eddy Simulation

DNS

Direct Numerical Simulation

RANS

Reynolds-Averaged Navier-Stokes

RST

Reynolds Stress Transport

STAR-CCM+

Simulation of Turbulent flows in Arbitrary Region - Computational Continuum Mechanics

EMP

Eulerian MultiPhase

VOF

Volume Of Fluid

DMP

Dispersed MultiPhase

MMP

Mixture MultiPhase

LMP

Lagrangian MultiPhase

DEM

Discrete Element Method

AMR

Adaptive Mesh Refinement

HEM

Homogeneous Equilibrium Model

HRM

Homogeneous Relaxation Model

AMG

Algebraic Multi-Grid

ELM

Edge Localized Mode

VDE

Vertical Displacement Event

RE

Runaway Electrons

VVPSS

Vacuum Vessel Pressure Suppression System

BD

Burst Disk

CFL

Courant-Friedrichs-Lewy

URF

Under-Relaxation Factor

CIWH

Condensation Induced Water Hammer

MTD

Minimum Temperature Distance

Symbols

Abbreviation	Description	Units
E	Energy	[J]
m	Mass	[kg]
c	Speed of light	[m/s]
η	Pressure ratio	[-]
p_{exit}	Exit pressure	[Pa]
p_{amb}	Ambient pressure	[Pa]
ρ	Density	[kg/m^3]
t	Time	[s]
$\mathbf{V}$	Velocity vector	[m/s]
p	Pressure	[Pa]
$\mathbf{b}$	Body force vector	[N/m^3]
τ	Viscous stress tensor	[N/m^2]
k	Kinetic energy	[J]
T	Temperature	[K]
S_E	Energy source	[J]
p_{in}	Inlet pressure	[Pa]
T_{in}	Inlet temperature	[K]
a	Average attraction between particles	[Pa·m^6/mol^2]
b	Volume excluded by a mole of particles	[m^3/mol]
V	Volume	[m^3]
R	Universal gas constant	[J/mol·K]
n	Number of moles	[mol]
Re	Reynolds number	[-]
v	Average velocity	[m/s]
L	Characteristic length	[m]
μ	Dynamic viscosity	[Pa·s]

Abbreviation	Description	Units
μ_t	Turbulent eddy viscosity	[m^2/s]
Y	Vapor mass fraction	[-]
$\overline{Y}$	Equilibrium mass fraction	[-]
Θ	Relaxation time scale	[s]
T_s	Static Temperature	[K]
T_t	Total Temperature	[K]
p_s	Static Pressure	[Pa]
p_t	Total Pressure	[Pa]
γ	Ratio of the specific heats	[-]
Ma	Mach number	[-]
D	Diameter	[m]
Kn	Knudsen number	[-]
λ	Molecular mean free path	[m]
k_B	Boltzmann constant	[J/K]
σ	Particle diameter	[m]
Δt	Time step	[s]
Δx	Length interval	[m]
δ	Cell size	[m]
δ_{min}	Minimum cell size	[m]
r	Radius	[m]
K	Constant due to the blockage nature	[-]
c_s	Speed of sound	[m/s]
v	Specific volume	[m^3/kg]
p_{avg}	Average pressure	[Pa]

Chapter 1

Introduction

1.1 Nuclear fusion

Nuclear fusion is the nuclear reaction that regulates the operation of stars and determines their lifetime. Contrary to nuclear fission, fusion occurs when two light nuclei fuse together to give rise to a new atom, releasing a substantial amount of energy in the form of heat. The amount of energy released by each reaction can be evaluated thanks to the Einstein's formula:

$$E = \Delta m c^2 \tag{1.1}$$

where Δm is the loss of mass, which represents the difference between the mass of the reagents and that of the products and c is the speed of light.

Nevertheless, in order to obtain this kind of reaction, an energy barrier must be overcome. This energy depends on the element taken into account and, in particular, on its cross section. As bigger atoms require more energy to be fused together, the best choice is to use very light atoms, such as two isotopes of hydrogen: deuterium (D) and tritium (T). Figure 1.1 shows the cross section of several fusion reactions as a function of the energy required to start the process.

As can be seen, the one that requires the lowest amount of energy is the D-T reaction:

$$\mathrm{D} + \mathrm{T} \longrightarrow {}^4\mathrm{He} + \mathrm{n} + 17.6\,\mathrm{MeV} \tag{1.2}$$

It is important to highlight that, on Earth, such energies can be obtained only at very high temperatures, (in the order of hundreds of millions of degrees) and in semi-vacuum conditions (order of µPa). Under these extreme conditions, the matter is in the fundamental state of plasma, which is nothing but an ionized gas with free ions and electrons (thanks to the high temperatures, the electrons are ripped away from the atom nucleus) within which fusion reactions take place. The energy released by these reactions can be used to produce electricity thanks to fusion reactors (e.g. stellarator, tokamak).

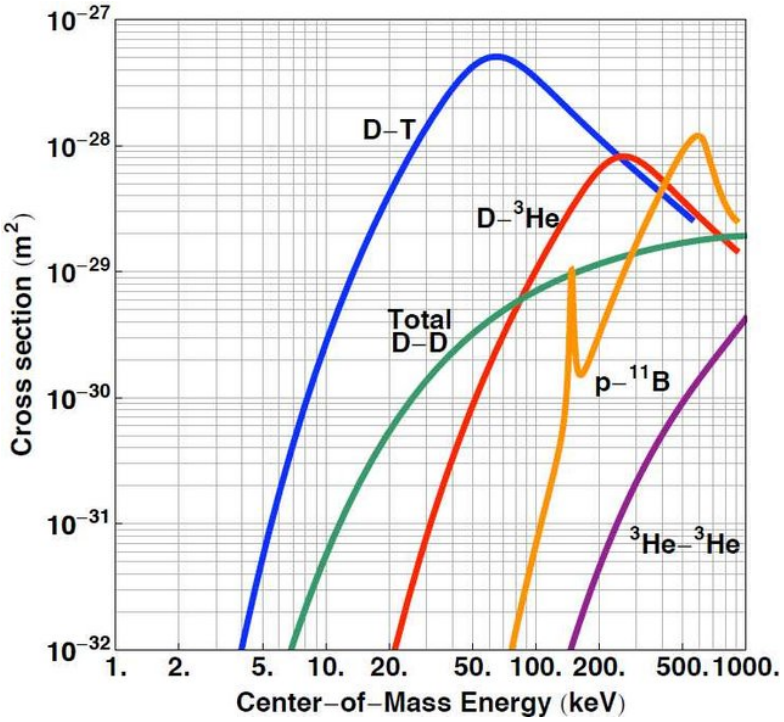

Figure 1.1: Cross section of different reactions as a function of the total energy of the system, reproduced from [1].

1.2 Tokamak

Among the different fusion reactor configurations proposed worldwide, the tokamak ("toroidal chamber with magnetic coils" from the russian translation) is the one which is being mainly developed by Europe. According to this reactor concept, the plasma is confined thanks to very strong magnetic fields in order to avoid direct interactions with the walls, since no known material is capable to withstand the contact with a fluid at such a high temperature.

In particular two different magnetic fields are generated (see figure 1.2): the "toroidal" field (TF) generated by the "toroidal field coils", which is directed along the torus and the "poloidal" field (PF), directed the short way around the torus and generated by the central solenoid. The two components result in a helical magnetic field that is able to confine the plasma, while another set of coils is used to give the plasma a shape and to fix its position.

The fusion reactions take place inside the plasma chamber (see figure 1.3), where the fuel (D-T) is injected and heated in order to reach the state of plasma, which is then confined by strong magnetic fields. Even if the plasma isn't in direct contact with the walls, it still subjects them to very strong thermal, mechanical, radiative

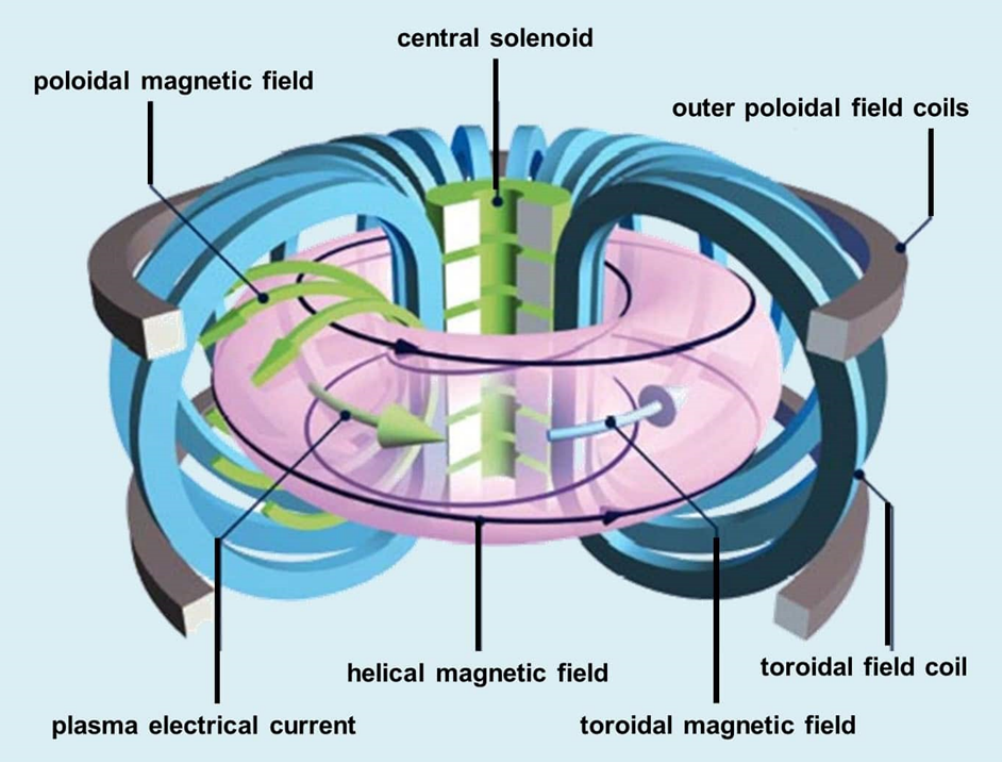

Figure 1.2: Magnetic fields inside a tokamak, courtesy of EUROfusion [2].

and neutronic loads, which must be properly managed [3].

The Breeding Blanket (BB) is the first component to see the plasma and it has three fundamental functions [3, 5]:

- Absorbing the energy deposited by the neutrons produced inside the plasma thanks to a suitable cooling system
- Shielding the outer components from the gamma rays and from the neutrons emitted by the plasma
- Using the high energy neutrons generated by the fusion reactions to produce Tritium from the Lithium stored inside the blanket.

Among the different BB concepts proposed worldwide, Europe is focusing on two main technologies: the Helium-Cooled Pebble Bed (HCPB) [6] and the Water-Cooled Lithium-Lead (WCLL) [7, 8]; the current work is based on the WCLL configuration, which foresees the use of sub-cooled water as a coolant.

The BB and the plasma chamber are both contained inside the Vacuum Vessel

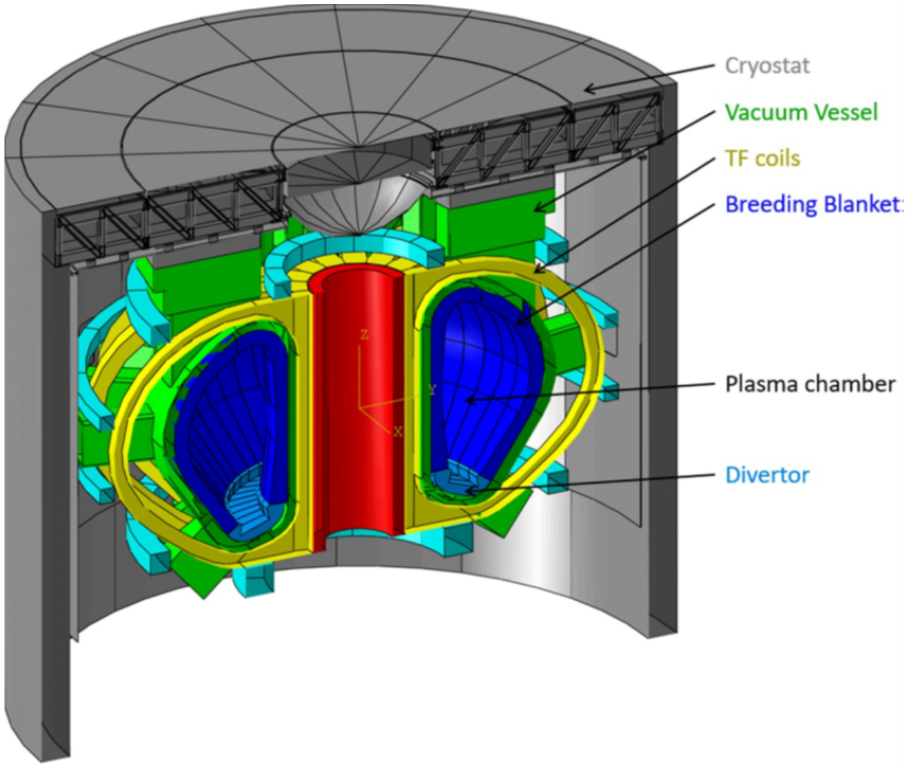

Figure 1.3: The EU DEMO tokamak [4].

(VV), a steel container, hermetically sealed, which provides a high-vacuum environment for the plasma and acts as a first safety barrier. The VV is then encapsulated inside the Cryostat, a massive stainless steel pressure chamber, that provides high-vacuum as well as the extreme cooling required by the superconducting magnets and the VV.

1.3 The WCLL Breeding Blanket

According to the current configuration, the WCLL-BB has been designed with a modular approach and it is subdivided in 16 different modules (one for each TF coil). The structural material adopted is EUROFER97, a ferritic-martensitic steel, while for both the neutron multiplier and the breeding material is used a Lithium-Lead alloy (Pb-Li) . Concerning the water cooling, it has been decided to employ two separate cooling systems: one for the First Wall (FW), which is the outermost layer of the breeding blanket facing the plasma and another one for the breeding zone, which is located more internally (see figure 1.4).

The FW plasma facing surface is covered with a 2 mm tungsten layer and it is

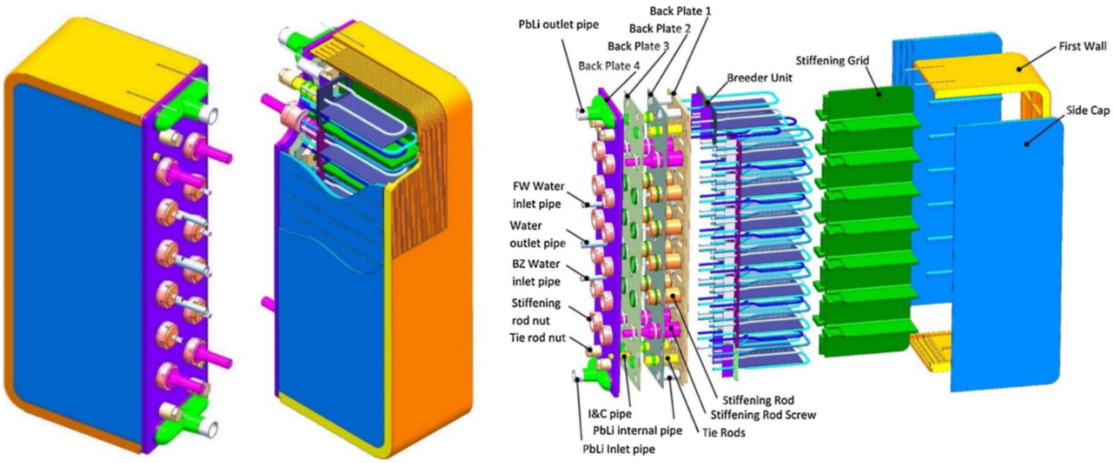

Figure 1.4: The WCLL blanket concept [9].

cooled by a system of 7 mm x 7 mm square channels, inside which water flows in counter-current direction. The breeding zone is instead cooled by water flowing in double-wall tubes [10] (see figure 1.5), which help reducing the probability of contact (with a consequent reaction) between the water and the Pb-Li alloy.

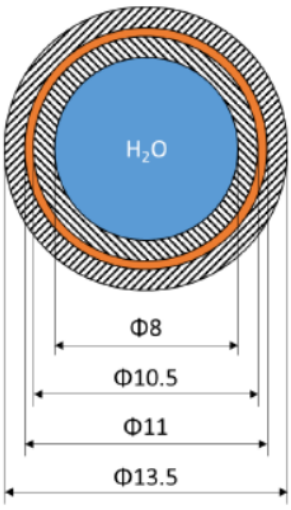

Figure 1.5: Double-walled tube [11].

In both systems the water thermodynamic conditions are equivalent to that of a Pressuirized Water Reactor (i.e. 155 bar, 295 °C÷328 °C).

1.4 EU DEMO

The experimental reactor currently under development in Cadarache, ITER (International Thermonuclear Experimental Reactor), will demonstrate the possibility to extract energy from fusion reactions, but it will not be connected to the grid. On the contrary, the construction of the EU DEMO reactor aims to demonstrate the capability of a fusion power plant to produce electricity for commercial uses. For this reason, it is important to pay particular attention to the safety of the plant already in its pre-conceptual design phase. As for all the nuclear reactors, the analysis of the so-called Design Basis Accidents (DBAs) is a critical aspect in the safety analysis. Among the different DBAs, one of the most representative is the Loss-Of-Coolant Accident, which usually occurs when a pipe breaks, causing the release of the coolant in the external environment.

1.5 LOCAs in fusion reactors

A LOCA can occur in different parts of a fusion reactor and, depending on the location, it will have different consequences. The two main components that can be involved in such an accident are the Breeding Blanket and the Superconducting Magnets.

- Breeding Blanket

  (a) **In-box LOCA**
  The failure occurs inside the blanket, more specifically in the breeding zone, leading (for the WCLL-BB concept) to the chemical interaction between Pb-Li and water. This exothermic reaction might cause a critical temperature and pressure increase. Furthermore, the pressure waves generated might propagate and damage the blanket structures.

  (b) **In-vessel LOCA**
  According to this scenario the rupture originates on the plasma-facing surface of the blanket, causing the release of pressurized coolant inside the plasma chamber. The thermodynamic conditions are such that the resulting jet might be sufficiently strong to compromise the structural integrity of the walls.

  (c) **Ex-vessel LOCA**
  This is the best known type of LOCA as it occurs under thermodynamic

conditions equivalent to those of a PWR. For this reason, it has been already extensively studied.

- Superconducting Magnets

  (a) **In-cryostat LOCA**
  The accident involves the release of helium coolant from one of the magnets into the cryostat. It is particularly dangerous as it can permanently damage the magnets, compromising their superconducting properties. It has some similarities with the in-vessel LOCA as they are both characterized by high pressure ratios and two-phase flow.

This work focuses on the analysis of a in-vessel LOCA (in-VV LOCA) for the WCLL-BB configuration.

1.6 In-VV LOCA

The in-VV LOCA originates when an unprotected plasma transient event occurs, causing an increase in the FW surface temperature that can lead to the failure of the component. During such an occurrence several cooling channels will be exposed, resulting in a release of pressurized water in the vacuum chamber [12]. Since the pressure difference between the cooling water and the chamber environment is very high, the water will undergo flash boiling at the exit of the pipe and a supersonic two-phase jet will be generated. This kind of accidents are usually modeled with system-level codes, such as RELAP [12, 13], GETTHEM [14, 15] or MELCOR [12, 16] which are able to analyze the behaviour of the entire system during the transient, adopting 0D/1D models of the main components. However, being based on a lumped approach, they are not able to evaluate localized quantities such as pressure peaks on the vessel walls, which must be considered in order to assess the cause of the failure. This is because, as opposed to fission reactors where the failure criterion is linked to a global parameter, the VV failure is directly related to the pressure on a specific surface (i.e., the gyrotron diamond windows). A full 3D transient Computational Fluid Dynamics (CFD) analysis is then necessary to compute the localized quantities of interest. This work aims to develop a CFD model able to describe the evolution of the transient, starting from the beginning of the accident, thus accounting for the phase change of the water.

1.7 Underexpanded jets

The underexpanded jet is a phenomenon that typically occurs at the exit of convergent-divergent nozzles, when the exit pressure is larger than the ambient

pressure [17]. The evolution of the jet depends on the pressure ratio:

$$\eta = \frac{p_{exit}}{p_{amb}} \tag{1.3}$$

The level of underexpansion has a significant impact on the flow pattern, according to the pressure ratio is indeed possible to distinguish between three different regimes [18]:

1. moderately underexpanded jets ($\eta <\sim 3$)
2. highly underexpanded jets ($2 < \eta < 4$)
3. very highly underexpanded jets ($\eta > 4$)

When the fluid reaches the exit plane with a pressure higher than the ambient pressure, it tries to compensate by expanding; the flow near the center keeps moving forward, while the one close to the nozzle edge turns outward, according to the so called Prandtl Meyer isoentropic expansion mechanism [19] (see figure 1.6). When the expansion waves reach the nozzle exit centerline, they are reflected back, toward the free jet boundary, where they are reflected inward again. The fluid that passes through these expansion waves is turned parallel to the centerline and reduced in pressure. If the pressure drops below p_{amb}, the reflected waves generate a compression fan, which may merge into an oblique shock [20]. At this point, the conditions of the flow are equivalent to that of the nozzle exit, so that the process may repeat itself, generating the characteristic repeated diamond pattern.

For highly underexpanded jets, the reflection of the oblique shock occurs after the intersection with a normal shock, called Mach disk [19]. The point where the oblique shock and the Mach disk intersect, is called triple point. From the triple point, both the reflected oblique shock and the slipstream are emanated. The latter, separates the subsonic flow downstream of the Mach disk from the supersonic flow upstream of the reflected shock. In case of very highly underexpanded jet ($\eta >> 4$), like the one considered in this work, the number of shock cells is reduced to one and the Mach disk becomes curved, as reported in figure 1.7, so it cannot be considered a normal shock anymore.

The phenomena discussed so far, are characteristic of steady underexpanded jet. However, the case under exam is focused on the beginning of a LOCA transient, thus the evolution of the jet must also be modeled, starting from the moment of the break. It is then important to describe the main phenomena expected during the first part of the transient, as they have been already investigated in [23, 24]. Right after the break, as the fluid starts exiting the pipe, a first shock starts to be generated (the so-called “Leading shock” or “Leading edge”) developing a planar front. The solid boundary of the rupture leads instead to the formation of an oblique shock, which soon after becomes the intercepting one, as it intercepts

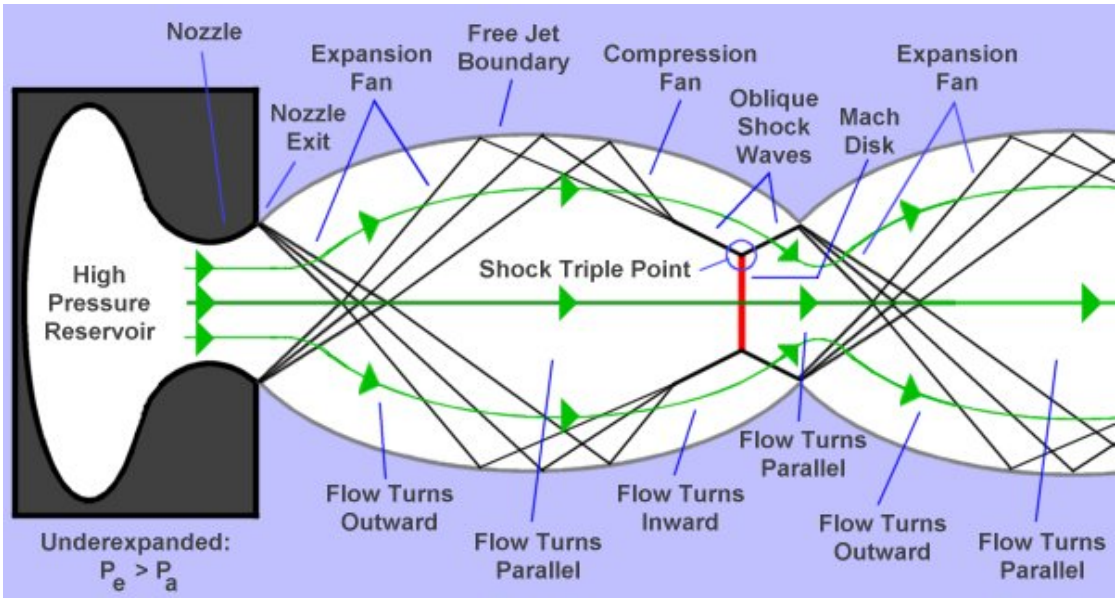

Figure 1.6: Diamonds pattern in an underexpanded jet. Reproduced from [21]

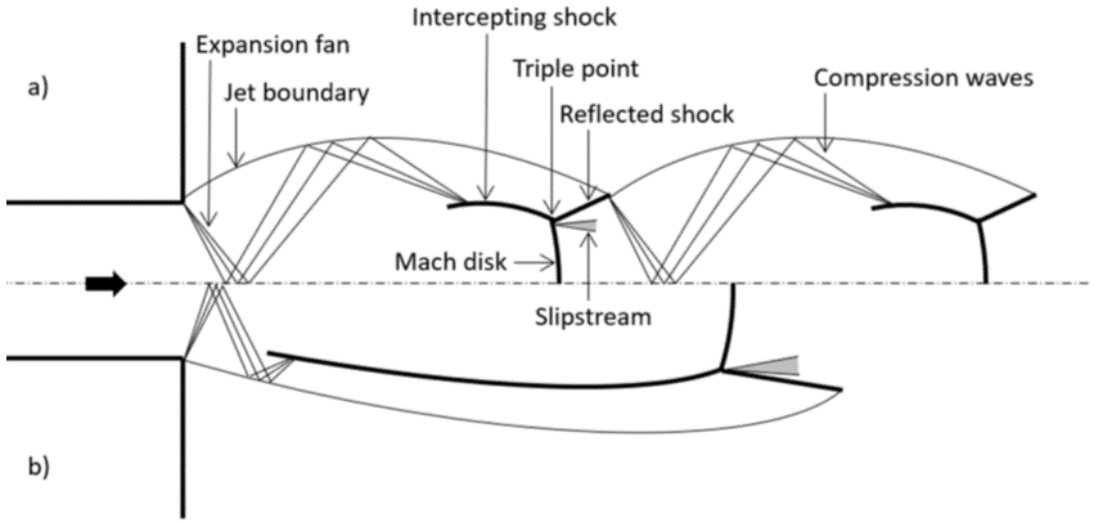

Figure 1.7: Structure of a (a) moderately and (b) very highly underexpanded jet. Taken from [22]

a second shock which is forming behind the leading edge. This shock will then propagate and grow, forming eventually the "Mach disk". As the jet evolution goes on, the leading shock will progressively dissipate, due to its expansion in a quiescent medium. On the contrary, the Mach disk will become stronger while

expanding, as the compression waves emanated from the rupture accumulates on it. After this moment, the presence of the wall in front of the rupture limits the jet evolution, which starts having a lower energetic content also thanks to the increase in the average pressure inside the VV, which in turn reduces the pressure ratio η.

1.8 Flashing jets

As already anticipated in section 1.6, the huge difference in pressure between the cooling water and the vacuum chamber will cause the water to boil instantly at the exit of the pipe, leading to the formation of a two-phase flashing jet (see figure 1.8). According to the initial conditions, the phase change mechanism can be different. If the fluid is at relatively low pressure and temperature, the "cavitation" phenomenon will take place; if the fluid is instead at high temperature and pressure, the so-called "flashing" phenomenon will occur, where the vaporization is limited by the heat transfer rate between the two phases [25]. During the flash boiling process, the formation and growth of the bubbles occurs in high thermal non-equilibrium conditions.

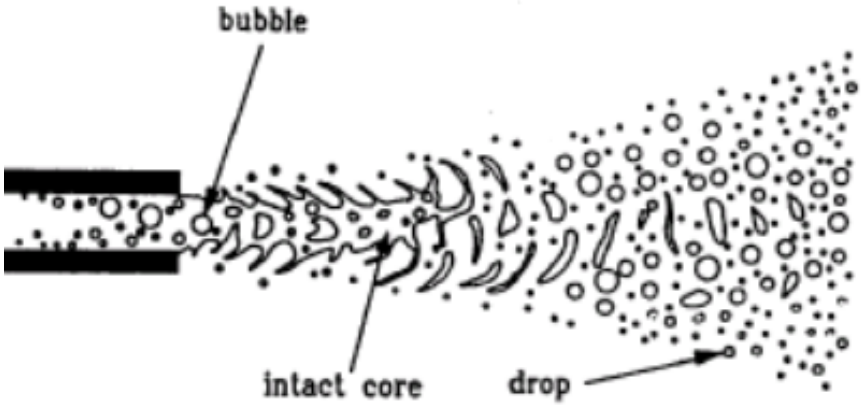

Figure 1.8: Representation of a flashing jet [26].

According to the upstream conditions of the fluid (total pressure and temperature, degree of superheat and turbulence), the flashing mechanism can occur inside the nozzle, leading to an explosive behaviour or at the nozzle exit, where the process is dominated by surface evaporation [27]. Another important difference with respect to single-phase jets, is that if the vaporization rate is fast enough to keep $\eta > 1$, the jet will be underexpanded even if the flow is not in chocked conditions [28]. In order to determine the thermal mechanisms occurring during the phase change, it

is important to analyze the thermodynamic of the flashing jet and in particular the degree of superheat of the fluid.
There are two possibilities:

- If the fluid has a low level of superheat, the mechanism which governs the phase change will be evaporation
- If the fluid has a high level of superheat, the driving mechanism will be boiling

The main difference is that evaporation is a surface phenomenon occurring when the fluid molecules have enough energy to make a transition from the liquid phase to the vapor phase. Boiling is instead a volume phenomenon and it occurs when the vapor pressure reaches the ambient value, allowing the formation of vapor bubbles inside the liquid.

Chapter 2

Modeling approach

2.1 Governing equations

The Navier-Stokes equations are the basic governing equations that describe the behaviour of a fluid flow. There are five main equations that combined together form the basis for numerical flow analysis: one for the conservation of mass (or "continuity equation"), three for the conservation of momentum and one for the conservation of energy.

2.1.1 Continuity equation

The mass conservation equation can be obtained by performing a mass balance on a control volume. It can be written in the following compact form:

$$\frac{\partial \rho}{\partial t} + \nabla \cdot (\rho \mathbf{V}) \;=\; 0 \tag{2.1}$$

where ρ is the density, t is the time and $\mathbf{V}$ the velocity vector.

2.1.2 Momentum equation

The momentum equation relates the rate of change of momentum of a control volume with the sum of the forces acting on the volume itself (for each of the three dimensions). It is an expression of Newton's second law and, as for the continuity, it can be written in a compact form:

$$\frac{\partial (\rho \mathbf{V})}{\partial t} + \nabla \cdot (\rho \mathbf{V}\mathbf{V}) \;=\; -\nabla p + \rho \mathbf{b} + \nabla \cdot \tau \tag{2.2}$$

Here ρ is the density, t is the time, $\mathbf{V}$ is the velocity vector, p is the pressure, $\mathbf{b}$ is the body forces vector and τ is the viscous stress tensor.

2.1.3 Energy equation

The energy conservation equation derives from the application of the first principle of thermodynamic on a control volume. Considering the total energy E as the sum of internal energy e and kinetic energy k, the energy balance can be expressed as follows:

$$\frac{\partial(\rho E)}{\partial t} + \nabla \cdot (\rho E \mathbf{V}) = -p\nabla \cdot \mathbf{V} + \nabla \cdot (k\nabla T) + \mathbf{b}\mathbf{V} + \nabla \cdot (\tau \mathbf{V}) + S_E \quad (2.3)$$

where ρ is the density, t is the time, $\mathbf{V}$ is the velocity vector, p is the pressure, $\mathbf{b}$ is the body forces vector, τ is the viscous stress tensor, k is the thermal conductivity, T is the temperature and S_E is an energy source.

2.1.4 Equations of state

The equations of state are constitutive relations that relate the two primary thermodynamic variables (i.e. pressure and temperature) to density and internal energy. Some of the available options are reported below.

Ideal gas

It is a good approximation for the behaviour of many gases, which are considered perfect gases. It can be used under many conditions, but it has several limitations. Usually it is written in the following form:

$$pV = nRT \quad (2.4)$$

where p is the pressure, V is the volume, n is the number of moles, R is the universal gas constant and T is the temperature.

Real gas

The p-v-T behaviour of a real gas at high pressure and low temperature, deviates from that predicted by the ideal gas law. This change in behaviour can be addressed to the molecules of the gas which, when the gas density increases, take up a significant portion of the total volume. Furthermore, the intermolecular attractive forces start becoming progressively more important. In order to take into account this additional volume occupied by the molecules, Van der Waals replaced the volume V in the ideal gas law with the term $(V - nb)$ and the pressure p with the term $(p + a\frac{n^2}{V^2})$, according to:

$$(p + a\frac{n^2}{V^2})(V - nb) = nRT \quad (2.5)$$

The new terms appearing in the equation, a and b, are two constants that consider the measure of the attractive forces and the co-volume of the particles, respectively.

IAPWS-IF97

Very often in CFD the thermodynamic properties of liquid water and steam are evaluated thanks to the IAPWS-IF97 ("International Association for the Properties of Water and Steam, Industrial Formulation 1997") library. The different thermodynamic properties of the fluid (e.g. specific volume, enthalpy, entropy, heat capacity, internal energy, speed of sound) are derived starting from a combination of the dimensionless Gibbs free energy and its derivatives. However, these models cannot be used always, but they have a certain range of applicability.

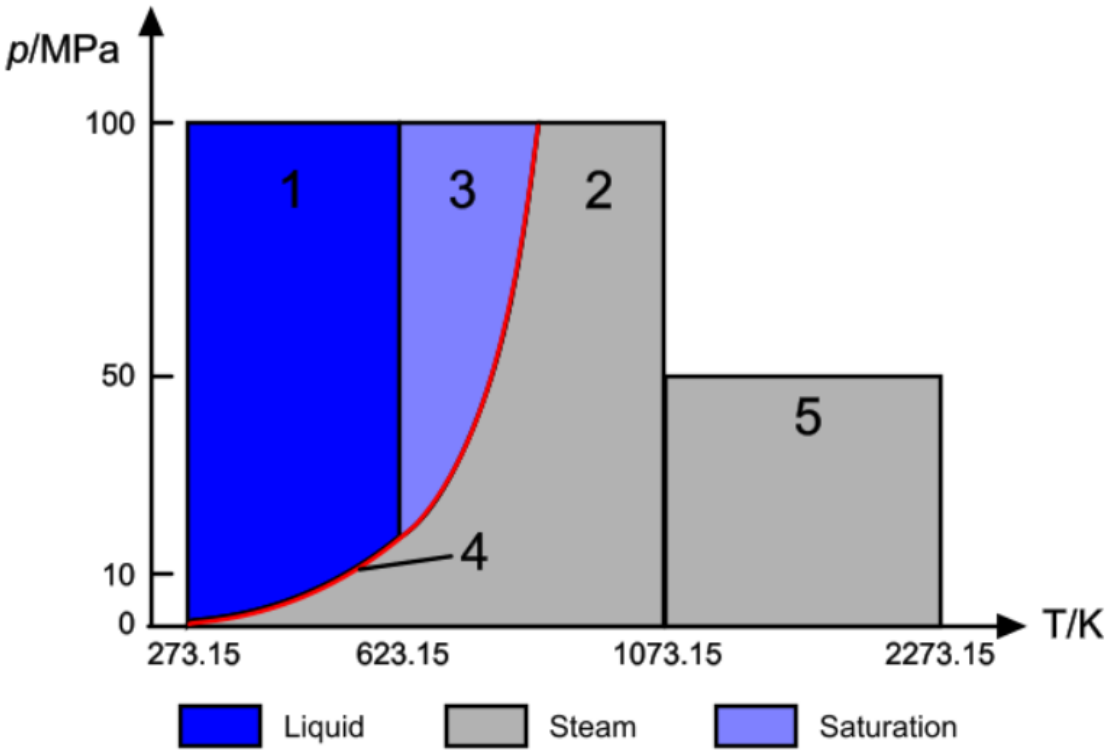

Figure 2.1: Different regions on the water p-T diagram according to the IAPWS-IF97 forumulation [29].

In the following table are resumed the validity ranges reported in figure 2.1:

Table 2.1: Validity range for each region [29].

Region	Temperature range [K]	Pressure range [MPa]
1-Liquid	273.15 ≤ T≤ 623.15	p≤100
2-Steam	273.15 ≤T≤ 1073.15	p≤100
3-Saturation	-	-
5-Steam	1073.15 ≤T≤ 2273.15	p≤50

2.1.5 Turbulence

The flow regime is a key parameter in the analysis of a flashing jet, as the effects of turbulence may strongly impact its characteristics. The Reynolds number is a dimensionless quantity that helps predict the fluid flow patterns in different situations. It is defined as the ratio between inertial forces and viscous forces according to:

$$Re = \frac{\rho \mathrm{v} L}{\mu} \tag{2.6}$$

where ρ is the density, L is the characteristic length, v is the average speed and μ is the dynamic viscosity of the fluid. At high Reynolds number the entrainment caused by turbulence increases, promoting the mixing of droplets inside the jet. It is therefore very important to properly model the turbulent effects by selecting the right numerical approach. Since the problem under exam is characterized by very high Reynolds number ($>1 \times 10^{10}$) and it has a huge computational domain ($\sim 750\,\mathrm{m}^3$), neither Large Eddy Simulation (LES) nor Direct Numerical Simulation (DNS) can be adopted, since they would require too much computational effort. The RANS method is therefore employed to simulate the accidental transient.

Reynolds-Averaged Navier-Stokes (RANS)

The RANS equations are obtained by applying the Reynolds decomposition to the Navier-Stokes equations. Each solution variable ϕ (e.g. pressure, velocity, energy) in the Navier-Stokes equations is decomposed into a mean value $\overline{\phi}$ and a fluctuating component ϕ'. Substituting the decomposed variables into the Navier-Stokes equations, results in a set of equations for the mean quantities, which are essentially identical to the original ones, except for an additional term that now appears in the momentum and energy transport equations. This additional term is the stress tensor, which must be solved in terms of mean flow quantities. Usually

two main approaches are adopted:

- **Eddy viscosity models**
  This models solve additional transport equations for scalar quantities that allow the turbulent eddy viscosity μ_t to be derived. Some example are:

  1. $k - \epsilon$ model
  2. $k - \omega$ model
  3. Spalart-Allmaras model

- **Reynolds stress transport (RST) models**
  The RST models compute directly the Reynolds stress tensor components by solving their governing transport equations.

2.1.6 Multiphase flow

For the purpose of carrying out a reliable numerical simulation, the transition among phases requires an appropriate mathematical model. The numerical modeling of such flows need to handle additional complexity with respect to single phase flows due to the presence of an interface between the two phases. The phases on either side of the interface have different chemical and physical properties and the exchange of mass, momentum and heat between the two, should be mathematically modeled as well. There are several types of multiphase fluid flows in literature that can be classified into three main fields (see figure 2.2):

1. Dispersed flows
2. Mixed flows
3. Stratified flows

Multiphase modeling in STAR-CCM+

The tool used in this work is STAR-CCM+ v.2021.2. It is a multiphysics computational fluid dynamics software that enables CFD engineers to model the complexity of products operating under real-world conditions. It is employed for a very wide range of simulations [29], including:

- Electromagnetic simulations
- Mechanical simulations
- Electrochemistry simulation

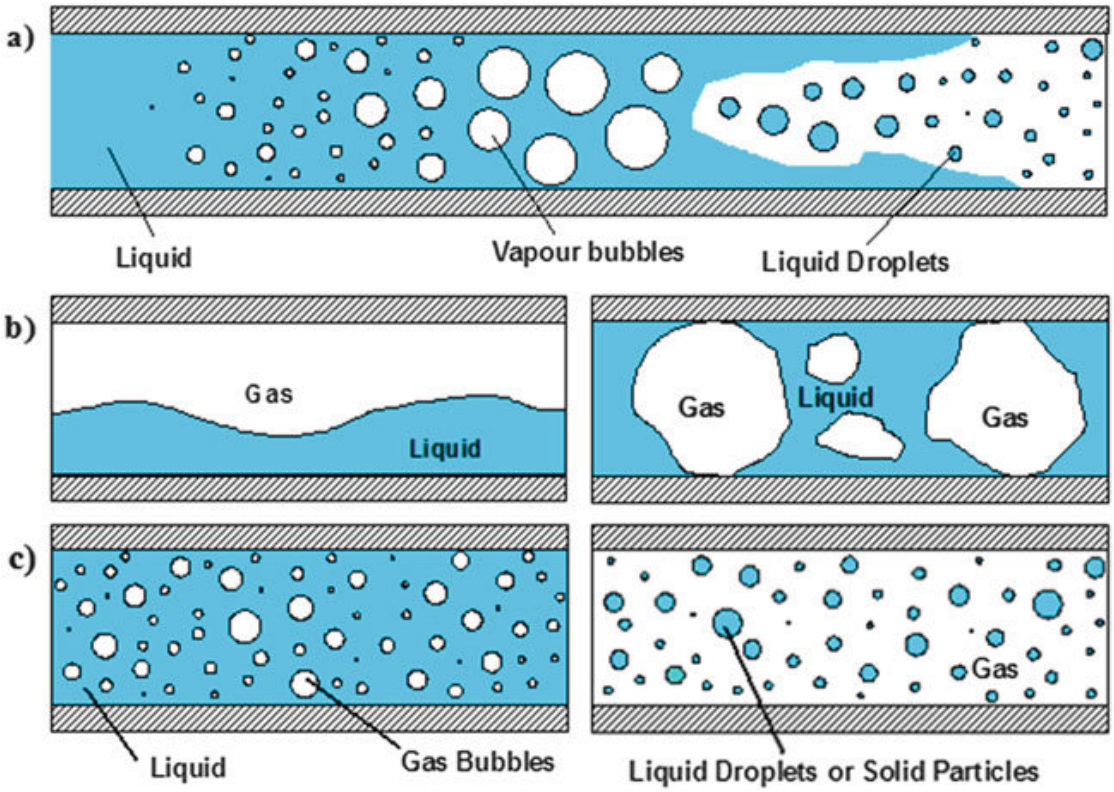

Figure 2.2: Different regimes of two-phase flows, (a) mixed or transient two-phase flow, (b) separated or stratified two-phase flow, (c) dispersed two-phase flow [30].

- Fluid simulations
- Multiphase flows simulations
- Engine simulation
- Particle flow integration

Concerning the multiphase flows simulations, the software offers different models that are able to cover basically all the multiphase regimes encountered in real world scenarios.

- **Eulerian Multiphase (EMP) Model**
  The EMP is a two-fluid model generally used for modeling dispersed flows. Each phase is treated as inter-penetrating continua, i.e. the two phases are mixed together on a length scale smaller than that of the computational mesh. The model solves continuity, momentum and energy equations of each phase, while the pressure field is shared between the phases. It also provides a flexible

framework where stratified or mixed two-phase flow can be modeled by using appropriate closure relations.

- **Volume Of Fluid (VOF) Model**
  The VOF model is an interface-capturing method that is generally used to predict the behaviour of the interface between immiscible phases. It uses a High-Resolution Interface Capturing (HRIC) scheme, which is specifically designed to track sharp interfaces. This multiphase model is also indicated to solve phase changes from liquid to vapor, such as evaporation, boiling, cavitation and flash boiling. When one of this vaporization mechanism is considered, it is important to select the thermal equilibrium condition more suitable for the case under exam. The two main options are: the Homogeneous Equilibrium Model (HEM) and the Homogeneous Relaxation Model (HRM). The HEM considers the two phases in thermal equilibrium ($T_l = T_g$) and assumes no relative velocities between them. This model has been used very often in flash boiling simulations due to its simplicity and low computational effort. However, it has been proved to give wrong results in case of short flow channels, where the time is insufficient for the two-phase mixture to reach equilibrium [31], like in the case analyzed in this work. The HRM tries to correct the HEM by introducing a finite rate equation for the rate of change of the vapor mass fraction with an empirical time-scale formulation, that makes it more suitable for cases characterized by thermal non-equilibrium conditions [29] (see [32] for a detailed comparison with other simpler models).
  The rate of change of vapor mass fraction is:

$$\frac{dY}{dt} = \frac{\overline{Y} - Y}{\Theta} \tag{2.7}$$

  where Y is the vapor mass fraction, $\overline{Y}$ is the equilibrium mass fraction and Θ is the relaxation time scale. Usually Θ is evaluated with the following correlation:

$$\Theta = \Theta_0 \alpha_v^{-0.54} \psi^{-1.76} \tag{2.8}$$

  where Θ_0 is a constant with value 3.84×10^{-7}, α_v is the vapor volume fraction and ψ is a non-dimensional pressure defined as:

$$\psi = \frac{p_{sat} - p}{p_{crit} - p_{sat}} \tag{2.9}$$

  Figure 2.3 shows the difference between HEM and HRM in the evaluation of the pressure evolution during a Super Canon experiment [32] (this experiment was carried out in order to reproduce the conditions of a LOCA originated by the sudden rupture of a steam pipe in a nuclear fission reactor).

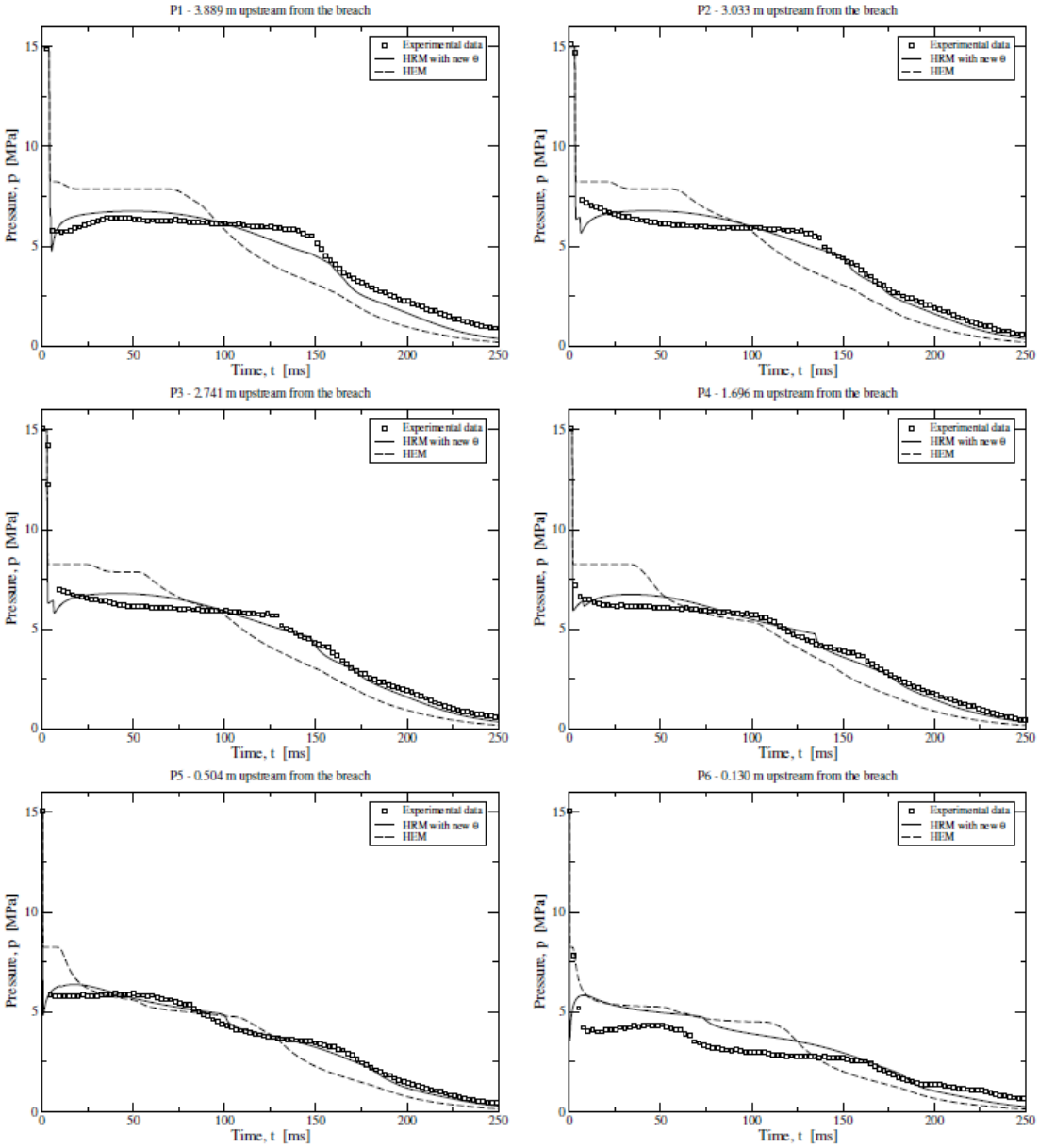

Figure 2.3: Assessment of HEM and HRM on a Super Canon experiment. The initial stagnation conditions are 15 MPa and 573.15 K [32].

- **Fluid Film Model**
  The Fluid Film model is used to simulate the distribution of a thin layer of liquid (the fluid film) on a solid surface. Its applications range from vehicle rainwater analysis to lubrication. It can also be used in conjunction with the

VOF model for a more flexible computation; the combination of these two models allows, in fact, to adopt the phase representation that is most suitable for the flow conditions and for the mesh resolution, depending on the case under exam.

- **Dispersed Multiphase (DMP) Model**
  The DMP model uses an Eulerian approach to simulate a disperse particle flow in a continuous phase. It is an alternative to the Lagrangian Multiphase models which, instead, uses a Lagrangian approach. By default, the two phases have a one-way interaction, which means that the continuous phase affects the dispersed phase, but not the other way around. However, a two-way model can be activated within DMP, which take into account the effects that the dispersed phase induces in the continuous phase.

- **Mixture Multiphase (MMP) Model**
  The MMP model considers the phases as miscible. It solves mass, momentum and energy equations for the whole mixture rather than considering each phase separately. The phases distribution is instead evaluated by solving the volume fraction transport equation for each phase. It is particularly indicated for modeling dispersed multiphase flows such as bubbly and droplet flows.

- **Lagrangian Multiphase (LMP) Model**
  The LMP model is used for simulations that involve a large number of particles, which are tracked by grouping into so-called parcels. It is suitable for dilute dispersed phases, with low volume fraction and little particle-particle collision. It can be one way or two way coupled with the flow.

- **Discrete Element Method (DEM)**
  The DEM is designed for modeling granular flow of materials such as sand, powders or food particles. Contrarily to the LMP model, it is employed to simulate fluid flows characterized by a high particle density and in which the particle-particle interactions are of relevance. It also takes into account the different shape and volumes of the particles other than spherical ones.

Chapter 3

Model Benchmark

The CFD model developed in this work is benchmarked against the results presented by Minato et al. in the technical report "Numerical Study of Two-Dimensional Structure in Critical Steam-Water Two-Phase Flow" [33]. The study deals with the release of a two dimensional two-phase flow from a vessel to an open space through a pipe, using the two-fluid model. The two main objectives are:

- Evaluation of the effect of multi-dimensional flow from a vessel into a pipe at critical discharge rate.
- Comparison of critical two-phase flow predictions by two-dimensional calculations with those by one-dimensional calculations.

Two cases are performed for 2D calculations: case A considers a flow area in the pipe and an open space in front of the pipe exit, while case B includes also the simulation of the flow from the large scale vessel into the pipe.

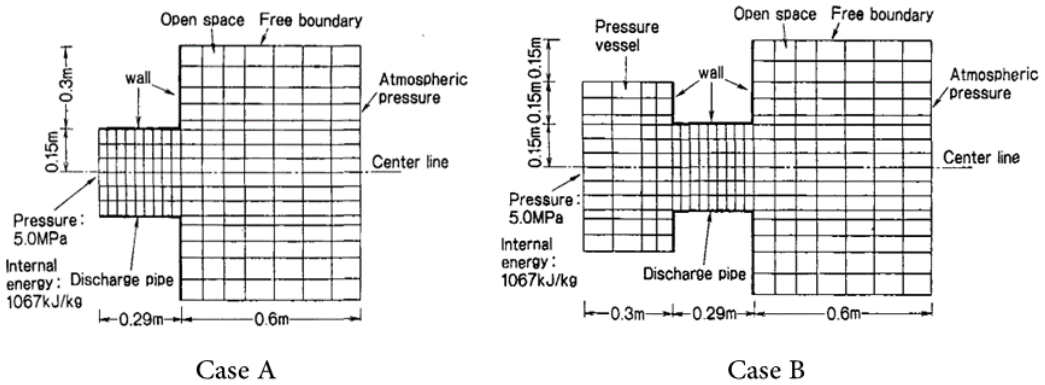

Figure 3.1: Control volumes for critical two-phase flow calculations [33].

Case B is then selected as a reference for the case of interest in this work, due to its similarities: it presents a simple computational domain which includes a vessel, a pipe and an open space, as reported in figure 3.1 and it also uses pressurized sub-cooled water as a working fluid, which undergoes flash boiling at the exit of the pipe.

3.1 Simulation setup

The domain proposed by Minato in [33], has been slightly modified in order to optimize the computational performances. First of all, an up-down symmetry has been exploited, allowing to halve the domain and thus reducing the computational cost. Then, the open space has been modified into a quarter circle shape, with a radius of 15 m, to allow the jet to develop undisturbed by what happens at the outlet. The modified domain together with the adopted boundary conditions are reported in figure 3.2.

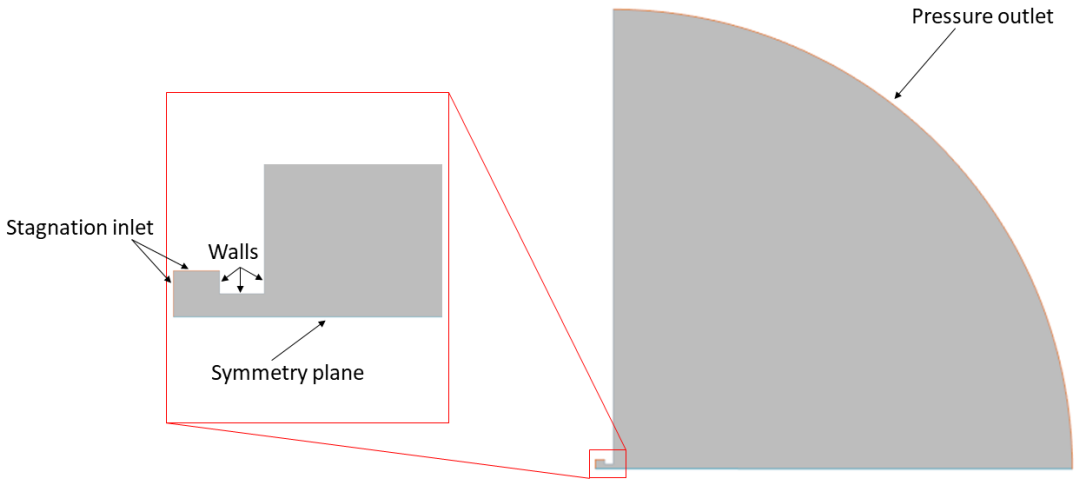

Figure 3.2: Computational domain and boundary conditions of the 2D case.

With reference to figure 3.2, the boundary conditions are listed below:

- **Inlet:** Assuming that the water inside the vessel is at rest (i.e. in stagnation conditions), the "stagnation inlet" boundary condition is selected. It asks for initial volume fraction, total pressure and temperature definitions, as well as for a supersonic static pressure, which is used only in the occurrence that the

flow at the inlet becomes sonic or supersonic. The initial values reported in table 3.1 are used as static values, while the total quantities are calculated according to:

$$\frac{p_t}{p_s} = \left(1 + \frac{\gamma - 1}{2}(Ma)^2\right)^{\frac{\gamma}{\gamma-1}} \tag{3.1}$$

where γ is the ratio of specific heats of the gas, and Ma is the Mach number (ratio between the fluid speed at the boundary and the speed of sound in the medium); as Ma is an output of the simulation, it is computed at each solver iteration on the inlet surface and substituted in equation 3.1.

$$\frac{T_t}{T_s} = 1 + \frac{\gamma - 1}{2}(Ma)^2 \tag{3.2}$$

Here T_s is the static temperature, and Ma is computed at each iteration as discussed above.

- **Outlet:** For the outlet, the "Pressure outlet" condition is selected, thus pressure, temperature and volume fraction must be prescribed.

- **Walls:** For the walls, the default setting are used (i.e. no slip, smooth and adiabatic)

- **Bottom boundary:** Thanks to the symmetry in the domain previously discussed, the "Symmetry plane" condition is applied to the lower boundary.

The initial conditions for pressure and temperature are reported in table 3.1, while in figure 3.3 is shown the initial distribution of volume fractions.

Table 3.1: Initial conditions of the 2D case [33].

Fluid	$\boldsymbol{T_{in}}$ **[K]**	$\boldsymbol{p_{in}}$ **[MPa]**
Water	519.1	5.0
Vapor	372.8	0.1

Being the initial expansion ratio (calculated with equation 1.3) equal to 50, the resulting two-phase jet will belong to the "very highly underexpanded jets" category (see section 1.7).

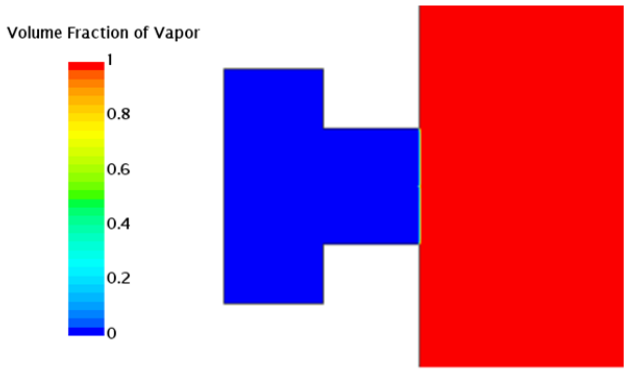

Figure 3.3: Initial volume fractions distribution.

3.2 Mesh

The creation of a suitable mesh is a fundamental step in any CFD analysis, as it significantly affects the results of the simulation. The problem at hand requires the computational domain to be finely discretized in order to catch the phase change mechanism occurring during the transient. Since the flashing phenomenon is expected to happen near the pipe exit, meshing very finely the entire domain would result in a waste of computational power, as the majority of the cells would unnecessarily solve an almost steady flow. A more efficient method is to employ very fine cells near the inlet region, which become progressively bigger moving towards the outlet.

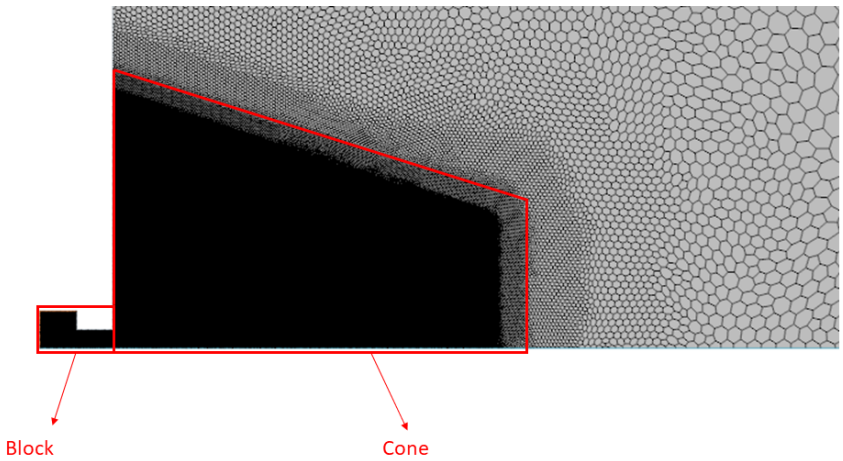

Figure 3.4: Static mesh adopted for the 2D model.

To do so, a volumetric custom control is employed: a block shape part is located in correspondence of the pipe, while a cone shape part is created to cover the portion of the domain which is expected to be occupied by the jet during the expansion process (see figure 3.4). The result of the static refinement is a mesh with approximately 288k total cells, which can be considered affordable for a 2D simulation. Nevertheless, employing a mesh refinement of this type would not be the best solution for a 3D simulation, as the additional number of cells due to the custom controls would increase sharply. The optimal choice would be an Adaptive Mesh Refinement (AMR) algorithm, which allows the mesh to adapt to the solution during the simulation. Unfortunately, the AMR solver already present in STAR-CCM+ can be used only for 3D simulations [29], making its use unfeasible for the 2D case under exam.

3.3 Model and Solvers

3.3.1 Models

The adopted models are listed below:

(a) **2D**
The 2D model is selected, since the reference work deals with a two-dimensional problem.

(b) **Multiphase**
The water is expected to undergo flash boiling at the exit of the pipe, thus a multiphase approach is necessary.

(c) **VOF**
The current problem requires first of all to properly model the phase change mechanisms occurring at the pipe exit, thus the choice of the multiphase model is a critical step. In this case the VOF model is selected for the reason discussed in 2.1.6. Furthermore, due to the high thermal non-equilibrium conditions at which flash-boiling takes place, the HRM model is enabled. The VOF model allows also the user to activate a compressibility enhancement option that improves the model's ability to solve highly compressible flows (Ma $>$ 0.3) [29].

(d) **Implicit unsteady**
Among the different options available to modeling time, the Implicit Unsteady model is the more stable and it is also the one with the largest applicability range.

(e) **Segregated flow**
When the VOF model is used, the software allows to select only the segregated flow model to solve the set of NS equations.

(f) **Segregated multiphase temperature**
When the energy equation is considered, the segregated temperature model is selected automatically together with the segregated flow model.

(g) **Turbulent (realisable k-ϵ two-layer)**
The flow regime is fully turbulent during the whole transient, thus the k-ϵ two-layer turbulence model is chosen, based on [29].

3.3.2 Solvers

Some solver need a suitable tuning in order to simulate the phenomenon in the best way possible.

1. **Implicit unsteady**
Its main function is to control the time-step size as well as the update at each physical time for the calculation. In particular, the time-step is chosen equal to 1 µs according to what reported by Minato in [33].

2. **Segregated flow and Segregated energy**
The discretization scheme is left with the default second-order upwind. However, the cycle employed in the Algebraic Multi-Grid (AMG) solver is switched from the default V-type to the F-type, which, as the W-type, performs better than the default one in supersonic conditions. In addition, it is also less expensive than the W-type from the computational point of view, representing a good compromise [29].

3.4 Results

The results of the simulation for three different time instants (1 ms - 10 ms - 40 ms) are illustrated below. In particular, a comparison with the results proposed by Minato et al. in [33] is carried out. However, since the paper doesn't provide explicit numerical data, the comparison can be performed only graphically, using a qualitative approach.

3.4.1 Void fraction

The distribution of the void fraction is shown in figure 3.5. The water coolant begins to flash at the pipe exit, where an interface between the the two-phase

mixture and the outgoing water is generated. Going on with the transient, the interface starts moving backwards and at around 10 ms a vapor annulus is formed near the pipe inlet. At 40 ms the interface reaches the vessel, generating a conical liquid core.

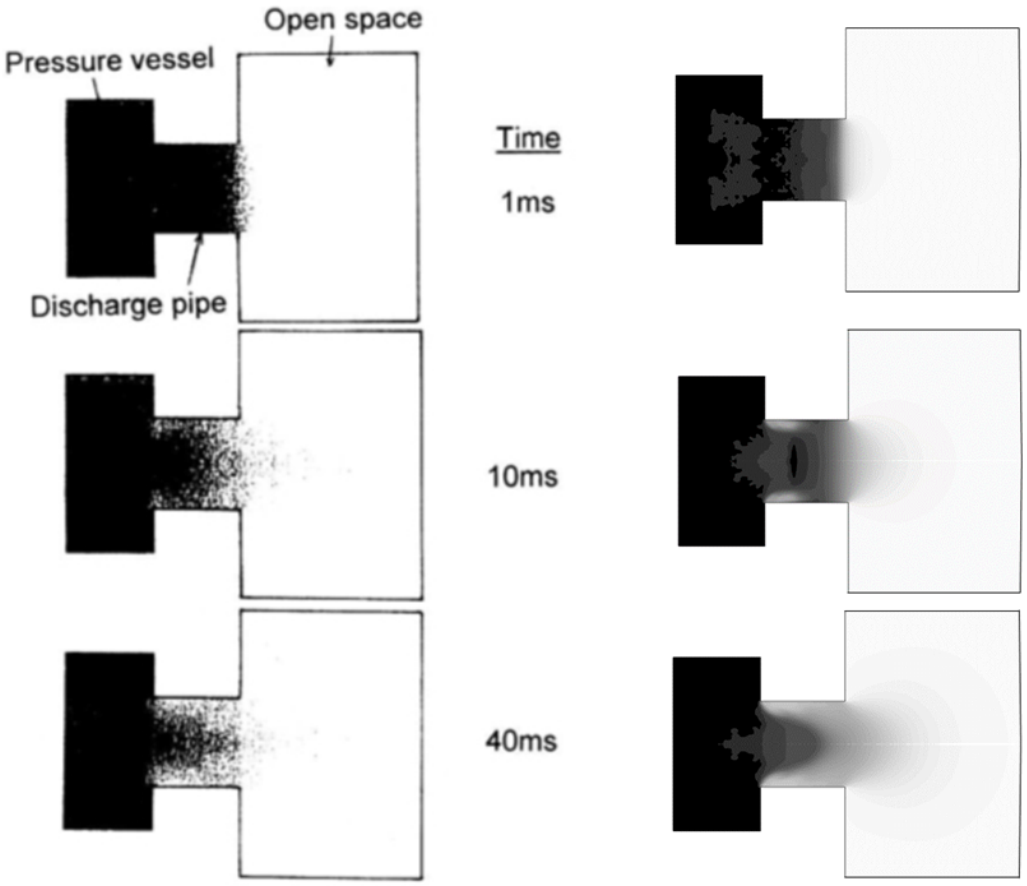

Figure 3.5: Void fraction distribution. Minato et al. [33] (left), this work (right).

3.4.2 Pressure

The pressure field is reported in figure 3.6. It can be seen how the pressure distribution is consistent with that of the void fraction, as the region characterized by the vapor annuls is at lower pressure with respect to the conical liquid core. Furthermore, a classic flashing jet behaviour can be observed, as the rapid volume expansion caused by the flashing mechanism at the pipe outlet, prevents the flow in the pipe to depressurize below ambient pressure.

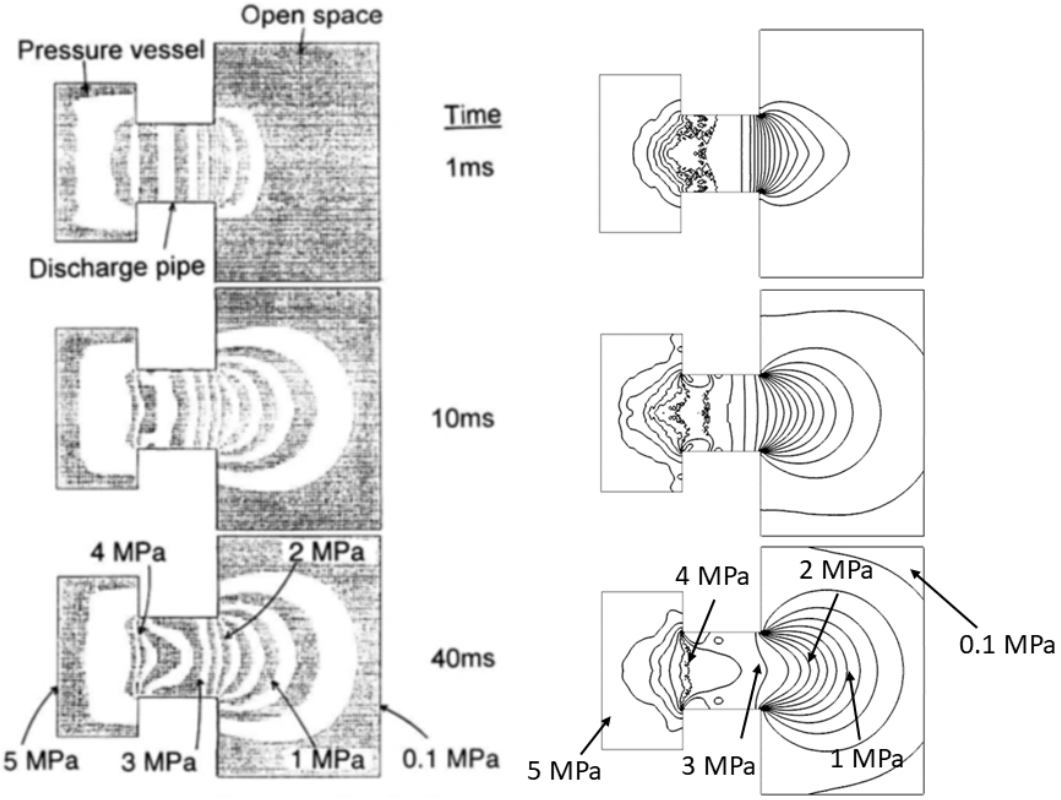

Figure 3.6: Pressure distribution. Minato et al. [33] (left), this work (right).

3.4.3 Velocity

Figure 3.7 and 3.8 present the velocity fields for the two different phases. In both figures the length of the arrows corresponds to the velocity magnitude. The velocity field of the liquid phase shows that the flow accelerates during the transient, as the arrows become progressively longer going from 1 ms to 40 ms. The gas velocity field, shows the occurrence of the flashing phenomenon at 1 ms. Furthermore, consistently with what discussed in 1.7, the flow undergoes an expansion process at the pipe exit, in order to compensate the pressure difference between the environment and the pressurized coolant.

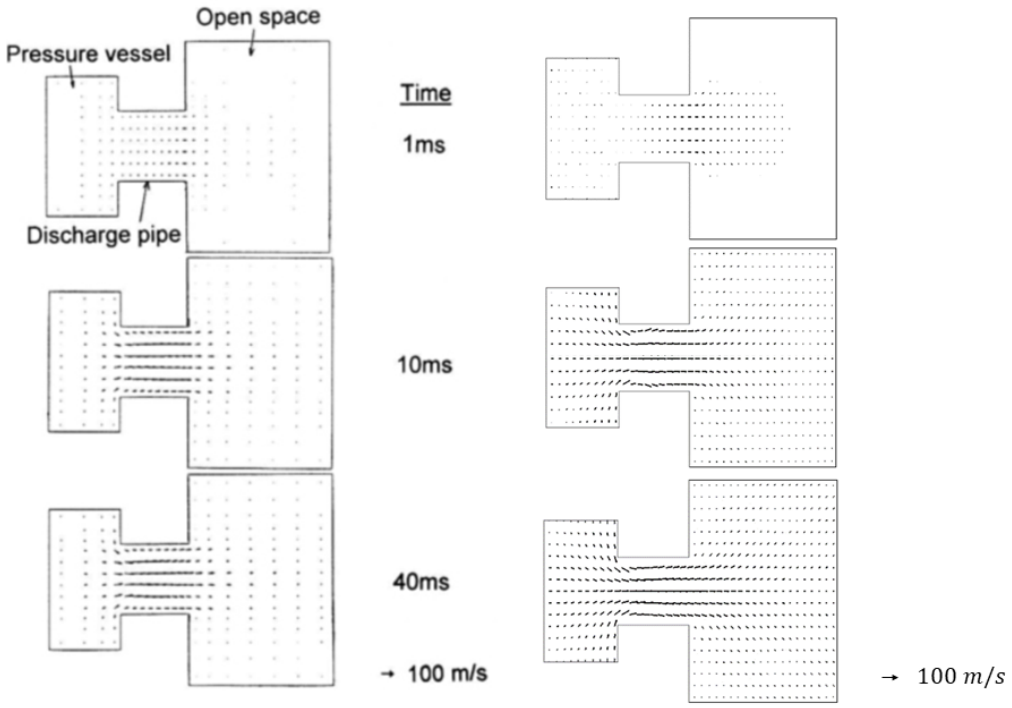

Figure 3.7: Velocity distribution of the liquid phase. Minato et al. [33] (left), this work (right).

3.4.4 Mass flow rate

The evolution of the mass flow rate at the pipe inlet is reported in figure 3.9. It shows a good level of agreement with the results proposed in [33] for the two-dimensional calculation of the case B, (see figure 3.10). In particular, the mass flow rate reaches an asymptotic value (steady discharge rate) after about 25 ms showing a little delay with respect to what reported in figure 3.10, as well as a slight overestimation of the steady discharge rate value.

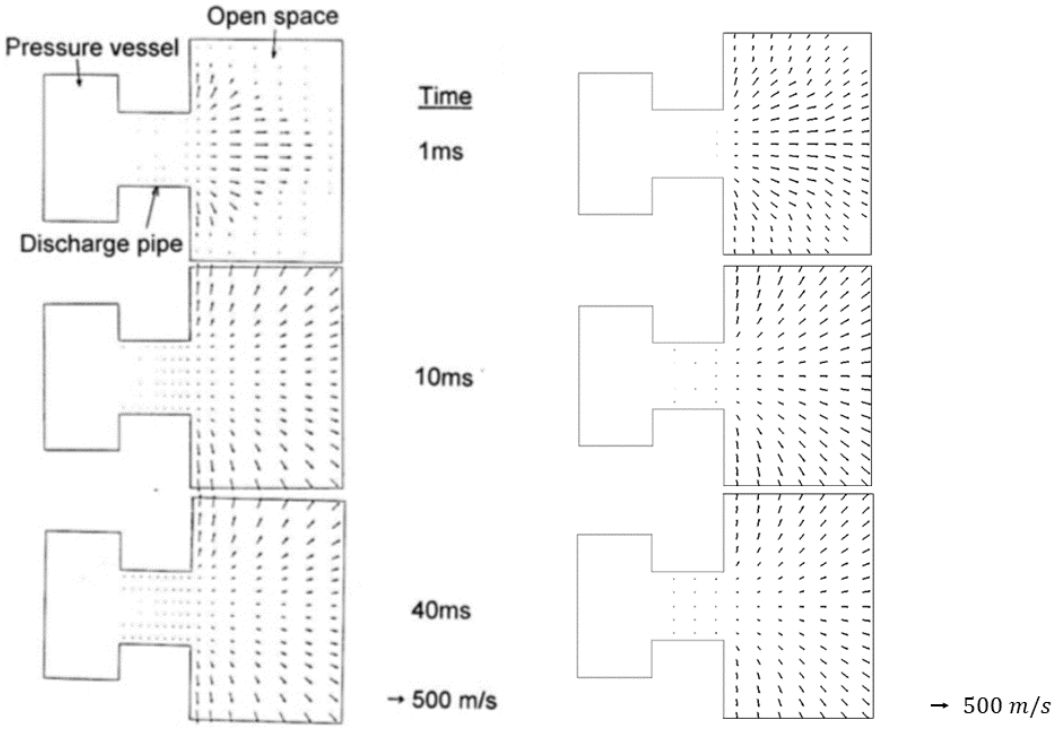

Figure 3.8: Velocity distribution of the gas phase. Minato et al. [33] (left), this work (right).

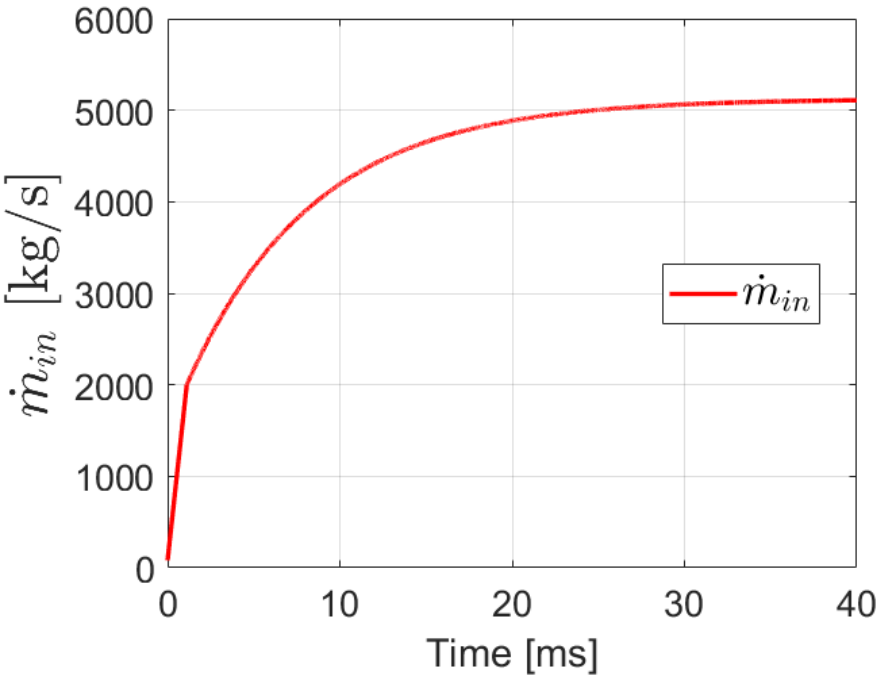

Figure 3.9: Mass flow rate evolution. This work.

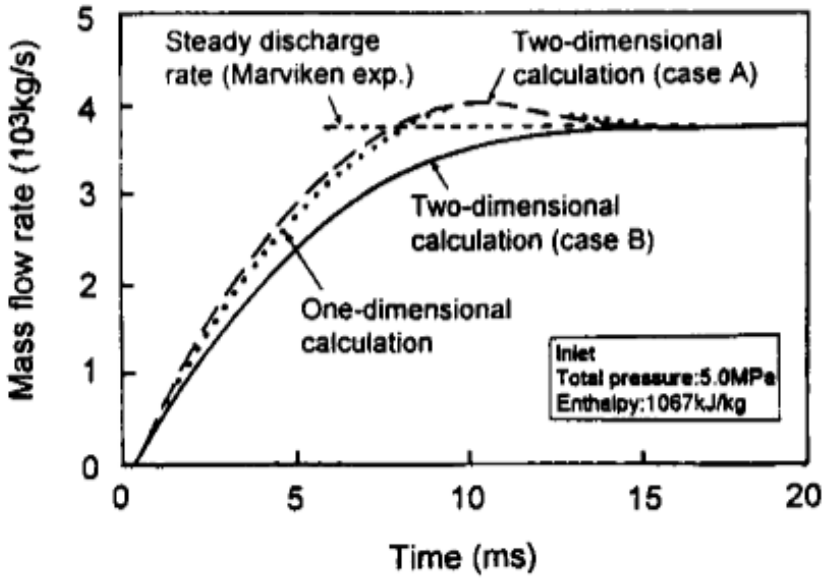

Figure 3.10: Mass flow rate evolution. Minato et al. [33]

Chapter 4

EU DEMO relevant case

The model previously developed is here applied and, where necessary, modified for a real-case scenario. In particular, the domain characteristics and the different thermodynamic conditions foreseen by the EU DEMO fusion reactor, require a suitable adaption of the model.

4.1 Scenario and geometry description

The accidental transient considered in this work is a Loss-Of-Coolant Accident inside the EU DEMO reactor Vacuum Vessel. The accident is initiated by a plasma transient event, such as edge localized modes (ELMs), vertical displacement events (VDEs), runaway electrons (RE), or disruptions. The occurrence of one of these transient may cause the plasma-facing surface temperature to increase very fast, leading eventually to the failure of the EUROFER97 structure. If a portion of the FW breaks, several cooling channel will remain uncovered, causing the coolant to be released inside the plasma chamber. According to the WCLL configuration, the released coolant would be water at 155 bar, 295 °C÷328 °C. Given the huge pressure difference with respect to the plasma chamber environment, a two-phase flashing jet will be generated (consistently with what discussed in section 1.8), whose effects on the vessel walls must be carefully analyzed. The design of the EU DEMO foresees a second environment, called Vacuum Vessel Pressure Suppression System (VVPSS), which is physically separated from the VV thanks to one or more Burst Disk (BD). Its main function is to mitigate the accidental consequences deriving from an event such the in-VV LOCA discussed here. Indeed, when the pressure on the disks surface reaches 1.5 bar, the BDs will automatically open, allowing the communication between the VV and the VVPSS. For this reason, the simulation carried out in this work begins at $t = 0$ s (i.e. with the occurrence of the break) and ends when the volume-averaged pressure inside the VV reaches 1.5 bar.

Furthermore, in order to consider the worst possible scenario, the break and the BD are located in toroidally opposite directions (i.e. at a toroidal distance of 180°) so that the distance travelled by the fluid is the maximum possible.

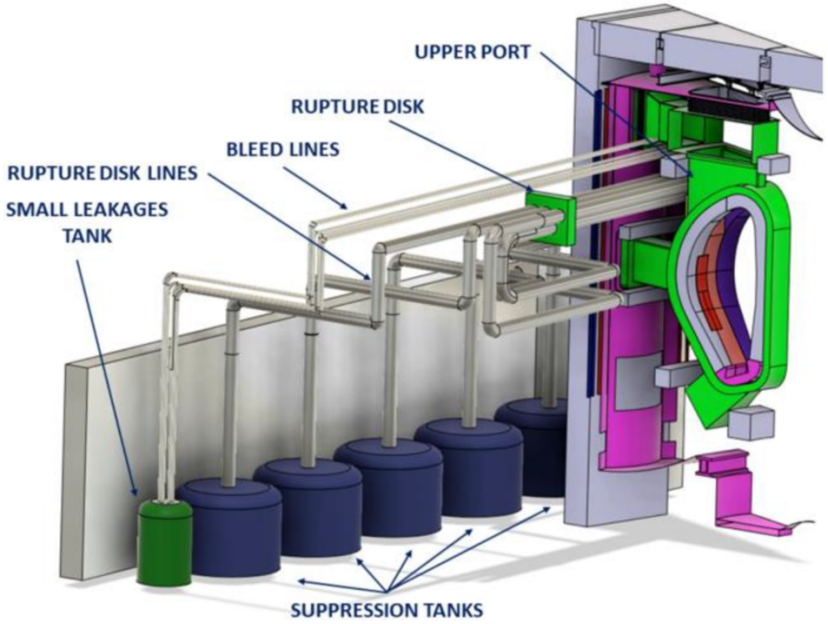

Figure 4.1: The VVPSS of the EU DEMO reactor [34].

Concerning the computational domain, a rigorous 3D analysis would require the entire free volume available in the VV to be considered. However, in order to reduce the computational effort, some simplifications are introduced:

(a) The flow in the gaps between the different Breeding Blanket segments is neglected, as it is considered not to impact the results of the simulation. For this reason, the fluid domain can be approximated with the main plasma chamber, allowing to exploit a left-right symmetry, which halves the initial domain.

(b) The presence of the divertor limits a possible up-down symmetry, nevertheless, in order to further reduce the domain, an up-down symmetric geometry is developed anyway. As a result, the final domain is equal to a fourth of the original one, with a volume equal to a fourth of the VV total volume ($\sim$750 m^3).

In figures 4.2, 4.3 and 4.4 the different steps required to build and simplify the computational domain are illustrated.

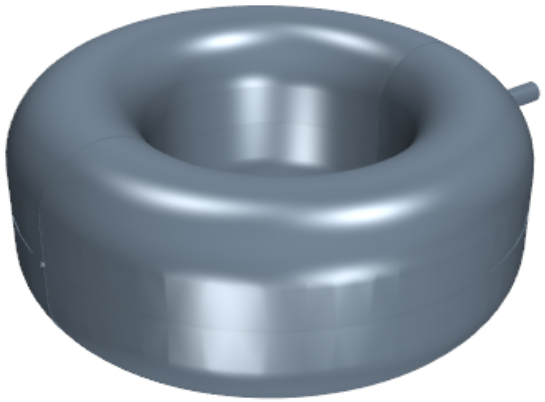

Figure 4.2: Full 3D domain without considering the divertor.

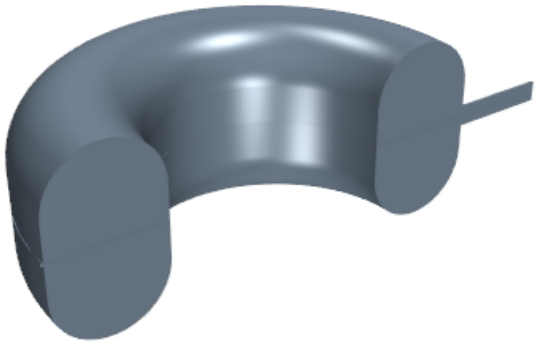

Figure 4.3: Computational domain after exploiting the left-right symmetry.

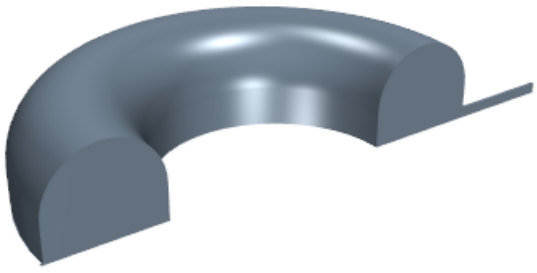

Figure 4.4: Computational domain after exploiting also the up-down symmetry.

According to the current scenario, a rupture area of $1\,\mathrm{m}^2$ is considered for the FW [7], which, considering the current design of the WCLL, would result in the breakage of 262 cooling channels [35]. To simplify the geometry, the inlet area is considered as twice the sum of all the channel sections to account also for the double-ended rupture. The resulting total area ($\sim 0.0308\ \mathrm{m}^2$) is used to evaluate the diameter (D) of an equivalent circular inlet region, according to:

$$\frac{D}{2} = \sqrt{\frac{0.0308}{\pi}} = 0.099\,\mathrm{m} \tag{4.1}$$

4.2 Simulation setup

The setup of the 3D transient CFD simulation is presented in this section.

4.2.1 Boundary and Initial Conditions

Boundary conditions

The adopted boundary conditions are shown in figure 4.5.

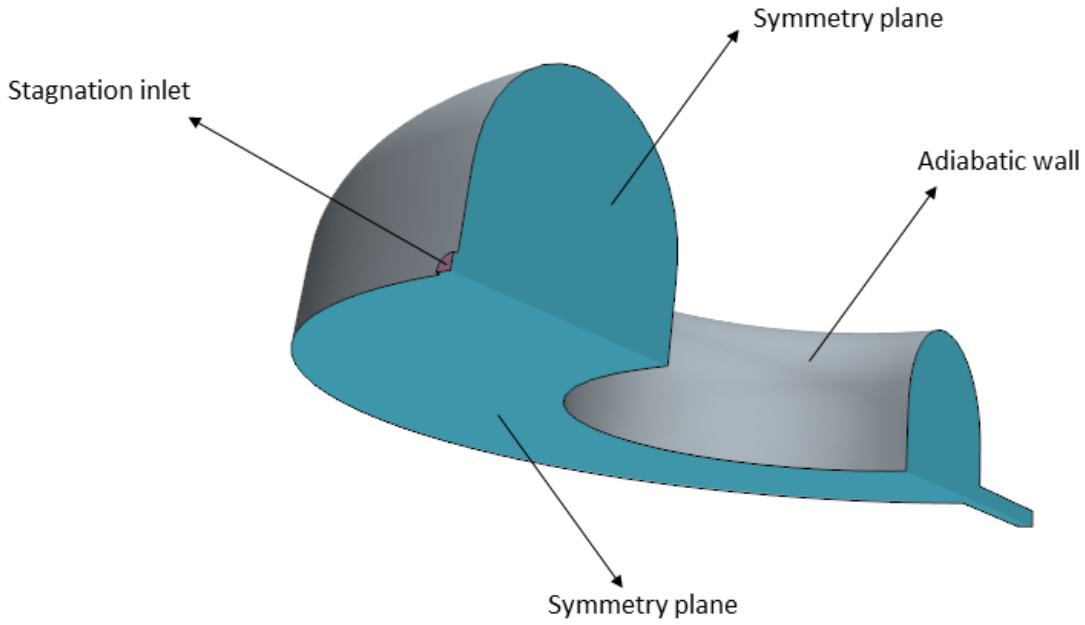

Figure 4.5: Computational domain and boundary conditions.

As already discussed in section 3.1, the "stagnation inlet" condition requires a specification for total temperature T_t, total pressure p_t and supersonic static pressure p_s. According to the scenario under exam, the value of T_s, used in equation 3.2 to compute T_t, is taken equal to 311.5 °C (mean value between 295 °C and 328 °C, i.e. inlet and outlet). On the other hand, the value of the static pressure is not so easy to assess, as it is affected by the time scale of the phenomenon. In this case, a constant inlet static pressure is chosen and it is set equal to the design value (155 bar), which is a conservative assumption as the very first instants of the transient, right after the break, cannot be modeled with CFD tools (see next section), and also because the depressurization of the system is not considered during the transient.

Similarly to what has been done in section 3.1, the boundary conditions for the wall and for the symmetry planes are left with the default settings.

Initial conditions

The initial conditions are resumed in table 4.1.

Table 4.1: Initial conditions of the 3D EU DEMO relevant case.

Fluid	$\boldsymbol{T_{in}}$ **[°C]**	$\boldsymbol{p_{in}}$ **[bar]**
Water	311.5	155
Vapor	45.8	0.1

Since it is not possible to leave empty the space inside the plasma chamber, the vessel domain is considered filled with water vapor. The actual value of pressure in operating conditions ranges from 1 Pa to 10 Pa, however, a pressure of 0.1 bar is selected as a reference value (leading to an initial pressure ratio of 1550). This choice is dictated by the flow regime, as CFD tools can only be used to model continuum phenomena, while for different types of flow, (e.g. free molecular flow), it is necessary to adopt a statistical approach. The parameter that allows to verify the flow regime is the Knudsen number, which is a dimensionless quantity defined as:

$$Kn = \frac{\lambda}{L} = \frac{k_B T}{\sqrt{2}\pi\sigma^2 p L} \tag{4.2}$$

where λ is the molecular mean free path, L is the characteristic length (in this case the distance between the inlet and the wall in front of it), k_B is the Boltzmann constant, T is the temperature of the system, σ is the particle diameter and p is the pressure of the system. Depending on the value of Kn, three different regimes can be identified [36]:

- $Kn < 0.001$: Continuum flow (No-slip boundary condition assumed for the walls)
- $0.001 < Kn < 0.1$: Slip flow (Slip boundary conditions is assumed)
- $Kn > 0.1$: Free molecular flow (Statistical methods are used to characterize the flow)

During the very first instants after the break, Kn is too high and the transient cannot be modeled with CFD (statistical methods such as Direct Simulation Monte Carlo would be necessary [37, 38]). This first part of the transient is therefore beyond the scope of this work.

For what regards the temperature conditions, instead, there is no knowledge of the actual values reached during an accident of this kind. However, several in-VV LOCA analyses performed with 0D tools, report initial VV temperature in the range of 290 K-600 K [16, 39, 40]. In addition, the initial conditions are shown to not affect the temperature evolution inside the VV [40].

4.2.2 Model and Solvers

Models

The models adopted for the 3D simulation are the same used for the analysis carried out in section 3.3.1, with some additions.

(a) **3D**
The domain is fully 3D, thus the 3D model is selected.

(b) **Adaptive time-step**
This model allows to change the time step during the simulation, according to some parameters defined by the user in the solvers settings.

(c) **Adaptive mesh**
An AMR algorithm is employed in order to optimize the number of cell required during the transient. It is computationally more efficient than a very fine static mesh (see section 4.2.3 for more details).

(d) **Solution interpolation**
For those cases in which the mesh changes during the simulation, this model allows to interpolate the solution data computed on the original mesh to the new one.

(e) **Multiphase**

(f) **VOF**
Also in this case the HRM model is enabled, as well as the compressibility enhancement option for flows characterized by Ma > 0.3

(g) **Implicit unsteady**

(h) **Segregated flow**

(i) **Segregated multiphase temperature**

(j) **Turbulent (realizable k-ϵ two-layer)**

Solvers

The solvers settings need to be adjusted for the real case application.

1. **Adaptive time-step**
The extreme difference between the coolant and the chamber thermodynamic conditions, makes the initial part of the transient the most critical time interval. Therefore, a time-step of 1×10^{-10} s is selected as first value. Nevertheless, after the jet start-up, this very small time-step is not needed anymore, thus a time-step adaptivity strategy based on the Courant-Friedrichs-Lewy (CFL) number is selected. The Courant number is a dimensionless parameter defined as:
$$CFL = \mathrm{v}\frac{\Delta t}{\Delta x} \tag{4.3}$$
where v is the local fluid velocity, Δt the time-step and Δx the cell size. It is a fundamental parameter in CFD for the numerical stability of the solution, as it relates the "real" velocity of the flow (v), with the "numerical" velocity ($\frac{\Delta x}{\Delta t}$). In particular, CFL > 1 means that the numerical solution is moving slower than the real flow, thus the fluid particles jump from a cell to another without passing through the ones in the middle. This condition, can lead to totally wrong solutions as the governing equations would not be respected. For this reason it is important to have the average CFL inside the domain < 1. The time-step adaptivity strategy employed asks for a maximum and an average CFL number to be specified. If both of them are below the imposed value (in this case $CFL_{Max} = 5.0$, $CFL_{Avg} = 0.5$) the time-step is increased by a factor 1.1, otherwise it is halved. The average time-step after the start-up is around 2 µs, while after the impact of the reflected pressure wave (see section 4.3.2) it increases to approximately 4 µs and it remains almost constant until the end.

2. **Implicit unsteady**
When the "Adaptive time-step" model is selected, this solver no longer control the time-step size. However, it allows to prescribe a maximum time-step

(dt_{max}), which is taken as a reference by the software. This means that the time-step cannot be larger than dt_{max} even if the CFL condition allows it.

3. **AMG linear solver**
   The AMG solver cycle is switched from V-type to F-type for all the selected solvers.

4. **Under-relaxation factors**
   All the under-relaxation factors (URF) are set to 0.1, except for those of velocity and pressure.

4.2.3 Mesh Adaptivity Strategy

As already mentioned in section 3.2, since different shock fronts are expected, the best way to mesh the domain is to employ an adaptive mesh, which is able to follow the shock fronts and, more generally, to adapt to the solution throughout the transient. The first step to build the mesh is choosing the type of volume mesher. The options available in STAR-CCM+ are the following:

- **Polyhedral mesher**
  It provides a balanced solution for complex mesh generation problems. It is generated starting from a tetrahedral mesh, but, in average, it requires five times less cell with respect to the tetrahedral one.

- **Tetrahedral mesher**
  It is the fastest among the three volume mesher and it also uses the least amount of memory for a given amount of cells. It provides an efficient and simple solution for complex mesh generation problems.

- **Trimmed cell mesher**
  It is a robust and efficient method, which is able to produce high quality grid for both complex and simple mesh generation problems. It is particularly good for external aerodynamic flows as it has the ability to refine the cells in a wake region.

A first choice would be to use the polyhedral mesher, as it would allow to spare some cells. However, it turns out that for problems characterized by very strong gradients, like the one under exam, the coupling between the built-in AMR solver and the polyhedral mesher introduces instabilities. Therefore, the tetrahedral mesher is selected among the three. The starting mesh needs to be very fine near the inlet and progressively coarser moving towards the opposite side of the torus. This is because the strong phase-change mechanism will take place in correspondence of the inlet, making it the most critical region in the entire domain as well as the

most accuracy-demanding area. To develop such a mesh, two sphere-shaped parts are generated and used as input parts for two different volumetric custom controls. The first sphere, reported in figure 4.6, has a radius (r) of 0.5 m and the average dimension of the cells inside it (δ) is equal to 0.005 m. The second sphere is instead bigger (r =3 m) and contains coarser cells (δ =0.05 m), as its main goal is to cover the area that will be occupied by the jet during the expansion process, thus the accuracy doesn't need to be too high (see figure 4.7).

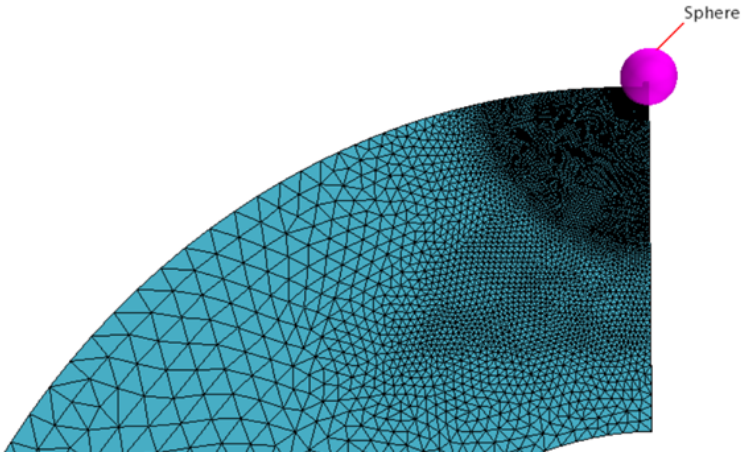

Figure 4.6: Small sphere used for the finer volumetric custom control.

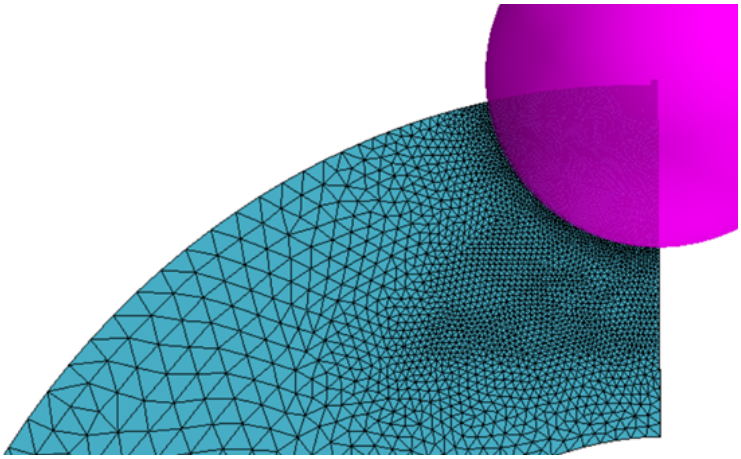

Figure 4.7: Big sphere used for the coarser volumetric custom control.

The next step is to set all the AMR solver properties so that the shock fronts can be properly followed. The refinement criterion is the most important parameter because it is the responsible of the adaption process. Two choices are offered by the software:

- **Free Surface Mesh Refinement**
  It refines the free surface separating two phases. It is very good in case of immiscible phases.

- **User-Defined Mesh Adaption**
  The user provide a field function (ϕ) or a table that will then drive the adaption process.

For the problem at hand the "User-Defined Mesh Adaption" is selected and the function used to drive the adaption (i.e. to catch the front propagation) is the Mach number variation ΔMa (see equation 4.4), similarly to what has been done in [22].

$$\phi = \Delta Ma = ||\nabla Ma||\ \delta \tag{4.4}$$

The refinement algorithm developed is the following:

1. The user defines a range for the AMR function ϕ, which in this case is [0.1,0.3].

2. Three different actions can be assigned to the solver: "Refine", "Keep" or "Coarsen".

3. According to the local value of the function ϕ in each cell, the solver performs the right action.

$$\begin{cases} \phi < 0.1 & coarsen \\ 0.1 \leq \phi \leq 0.3 & keep \\ \phi > 0.3 & refine \end{cases} \tag{4.5}$$

Two other important parameters used to limit or stop the refinement process are "Limit cell size" and "Maximum refinement level". The first one allows the user to impose a minimum cell size value δ_{min} (in this case 0.01 m), below which it is not possible to go. The second one instead, fixes the maximum number of times that a given cell can be refined by the AMR solver.

The resulting mesh is presented in figure 4.8 respectively after $t = 7$ ms and $t = 17$ ms of simulation. It is possible to notice both the refinement spheres, as well as the adapted mesh which follows the different fronts, represented by the two refined bands.

Thanks to this dynamic mesh, the number of cells is kept below 12 million for the whole simulation. In particular, a first reduction from $\sim 12M$ cells to $\sim 10M$ cells is experienced after the impact with the front wall, while, following the impact of the reflected pressure wave (see section 4.3.2), the number of cells drastically drop down to $\sim 1M$ allowing to significantly speed up the computation.

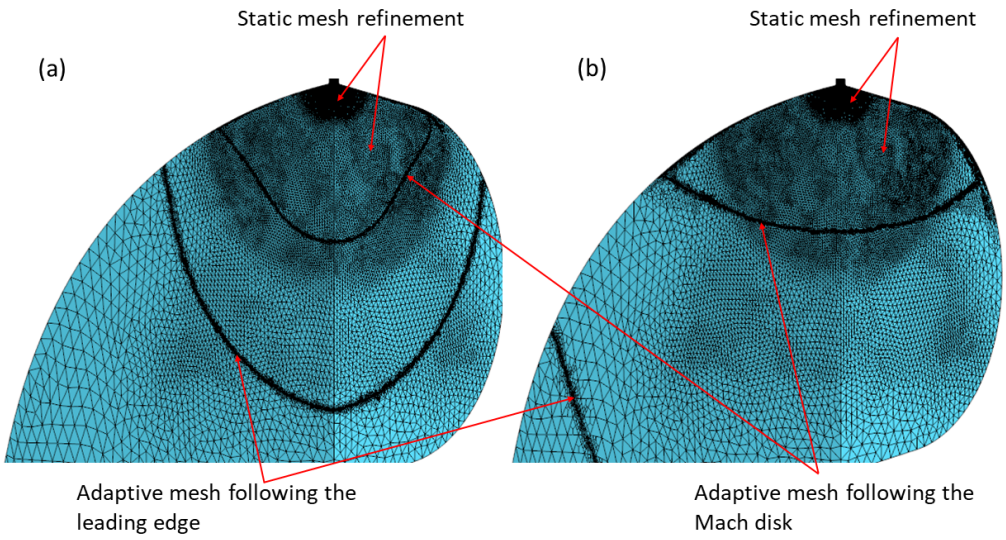

Figure 4.8: Adaptive mesh details at (a) 7.0 ms and (b) 17.0 ms.

4.3 Results

The results of the CFD simulation are presented in this section.

4.3.1 Flow Field

The first instants of the jet evolution are shown in figure 4.9. Right after the break, the jet develops a planar front (see figure 4.9a) since it is not yet affected by the shape of the rupture. Then, as the flashing mechanism takes place at the pipe outlet, the generated vapor is pushed in all directions leading to the formation of a spherical front (see figure 4.9b). After few ms of expansion, it's already possible to notice the distinction between the leading shock and the Mach disk (see figure 4.9c), consistently with what discussed in section 1.7. The moment of the impact between the leading edge and the VV inboard wall is shown in figure 4.9f.

The jet evolution after the impact is presented in figure 4.10. When the leading shock hits the front wall, it causes a sharp pressure increase on the wall surface (see also section 4.3.2). From that point, a reflected pressure wave is generated and it starts moving backwards, where it finds the Mack disk that is still propagating behind the leading edge. The direct consequence of the interaction between the pressure wave and the Mach disk, is that the latter starts to be compressed and thus deformed. In particular, it spreads along the radial direction and narrows along the axial direction, as can be seen in figure 4.10a-c. Going on with the

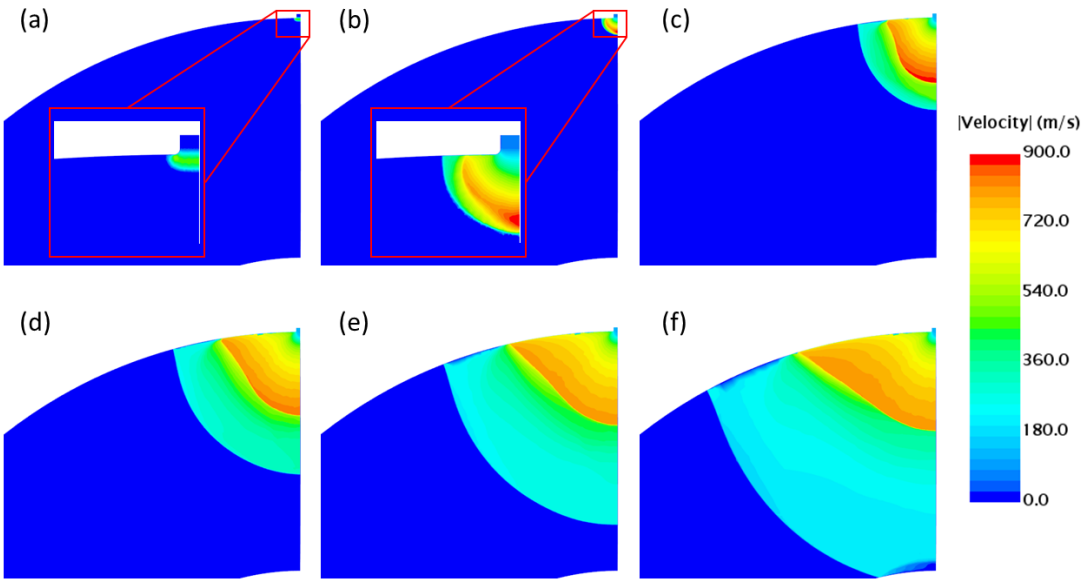

Figure 4.9: Flow field evolution before the impact with the front wall at (a) 0.1 ms, (b) 0.5 ms, (c) 3.0 ms, (d) 5.0 ms, (e) 7.0 ms and (f) 9.5 ms.

transient, the Mach disk does not withstand the pressure exerted by the reflected wave, which strongly deforms the Mach disk up to the point that it completely dissipates at $t = 55$ ms (see figure 4.10f).

Figure 4.11 shows the evolution of the jet far after the impact with the front wall. As can be seen in figure 4.11a-c, a second Mack disk is generated and it grows according to the distinctive features of underexpanded jets. Nevertheless, this second jet is much less energetic with respect to the first one. This is because, in the meanwhile, the average pressure inside the VV is increased, which means that the pressure ratio is much smaller and does not lead to a violent expansion like in the initial part of the transient. Around $t = 600.0$ ms, the Mach disk stabilizes and a slipstream is generated (see figure 4.11e-f), similarly to what was observed in [22] for the Helium-cooled BB case. From this moment on, no additional scalar scenes are presented, as the jet stabilizes giving no additional information. It is also interesting to notice that, according to what reported in [18], the position of the shock front at $t = 600.0$ ms, in steady regime, should be approximately at 2.3 m from the pipe exit, which is not that far from what shown in figure 4.11f, where the Mack disk expands from the pipe outlet for ~ 2.7 m. However, it's important to highlight that the comparison can be performed only in a qualitative way, since the phenomena under exam is of transient nature, while the work carried out in [18] is valid for steady-state jets only.

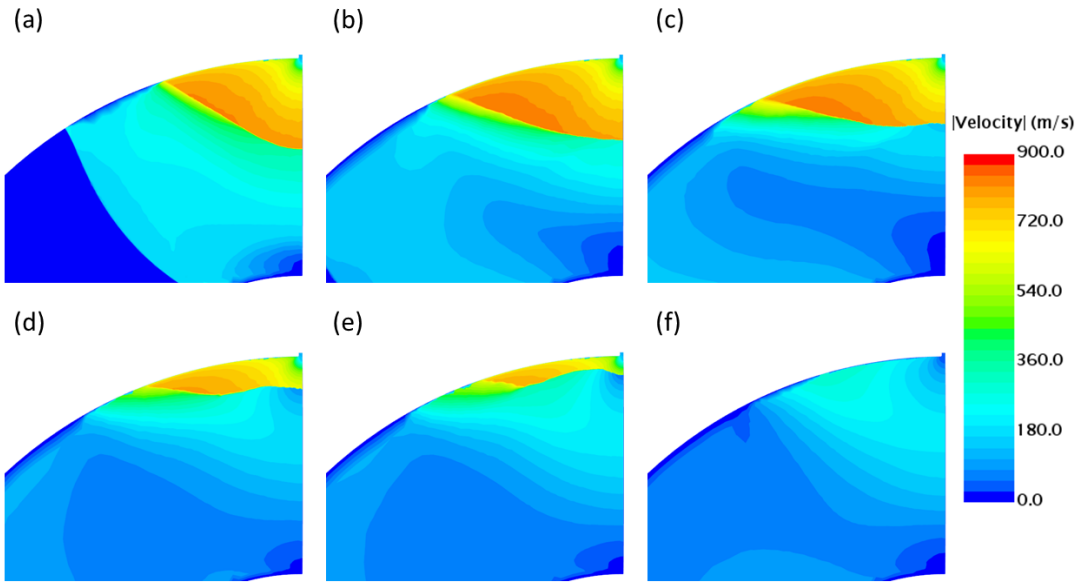

Figure 4.10: Flow field evolution after the impact with the front wall at (a) 11.0 ms, (b) 17.0 ms, (c) 25.0 ms, (d) 40.0 ms, (e) 45.0 ms and (f) 55.0 ms.

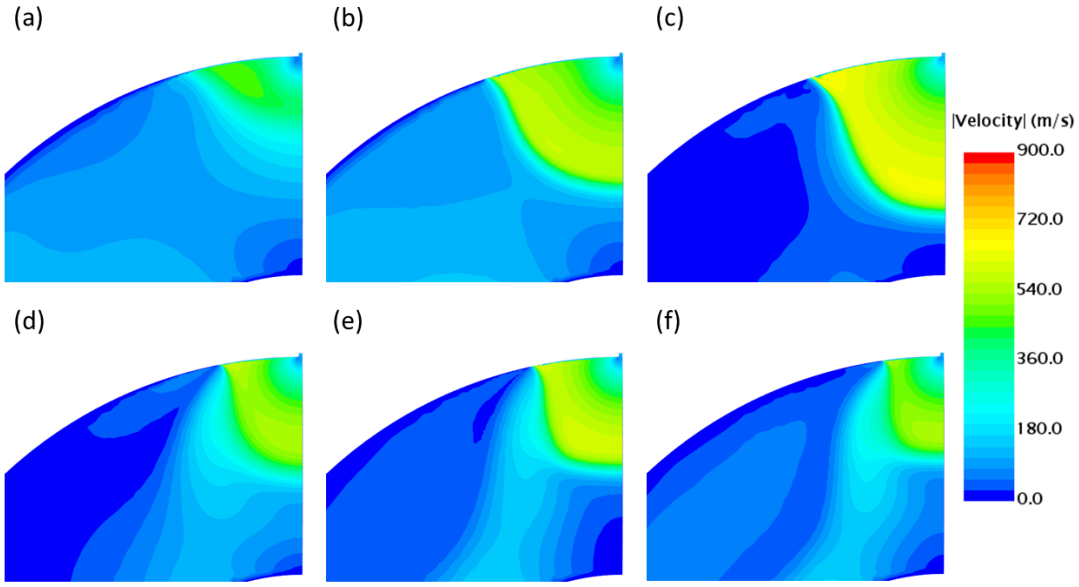

Figure 4.11: Flow field evolution far after the impact with the front wall at (a) 170.0 ms, (b) 200.0 ms, (c) 270.0 ms, (d) 310.0 ms, (e) 400.0 ms and (f) 590.0 ms.

4.3.2 Pressure Evolution and Void Fraction

The pressure evolution as well as the phase change mechanisms are monitored throughout the transient in order to analyze the effects induced by the pressure wave as it moves inside the torus. In particular, two points are used as a reference for the analysis: the "Outboard" point, located in the inlet region and the "Inboard" point, located near the front wall (see figure 4.12).

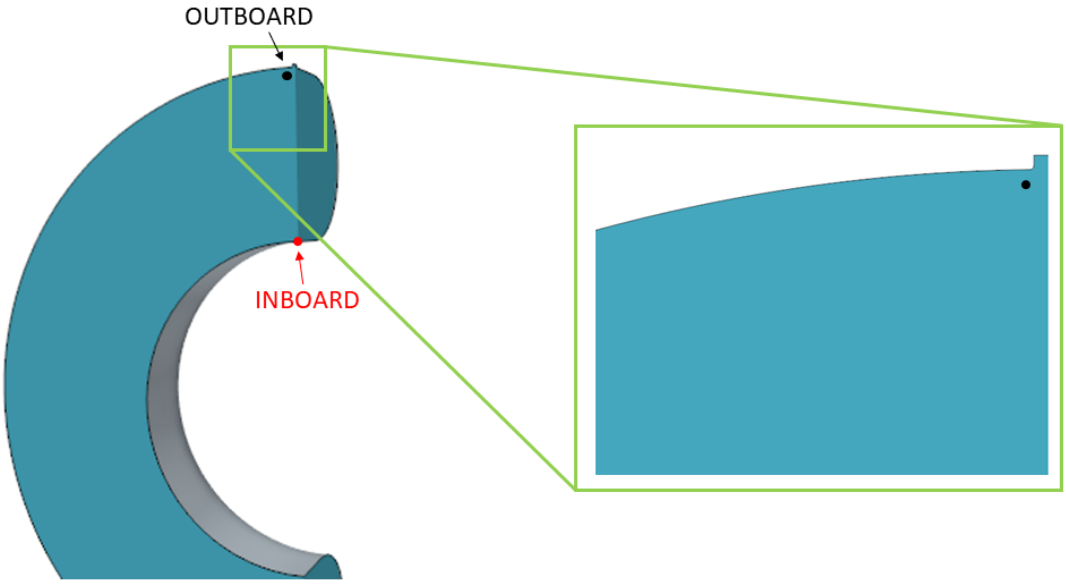

Figure 4.12: Significant points used to monitor pressure evolution and void fraction.

Figure 4.13 shows the pressure evolution of the points mentioned above. The impact of the leading edge with the front wall can be immediately noticed, as it is represented by the spike in the "Inboard" point evolution. Indeed the pressure increases from 0.1 bar to $\sim$ 0.35 bar, showing that the collision is not a threat for the structural integrity of the material.

Going on with the transient, the inlet area becomes instead the most interesting one. This is because, as anticipated in section 4.3.1, a reflected pressure wave is generated after the impact with the front wall and it starts traveling towards the inlet. Figure 4.14, shows the pressure profile along the symmetry axis for different time instants. It is worth highlighting the shift in the shock front (represented by the local pressure peak) as the wave passes by, which shows how the wave changes direction. Before the impact, the peak moves from z $\sim$ 2.35 m to z $\sim$ 2.50 m (from the blue line to the red line), so it is moving forward. After the impact instead, which occur at 9.5 ms, the peak is clearly moving backward, as it goes from z

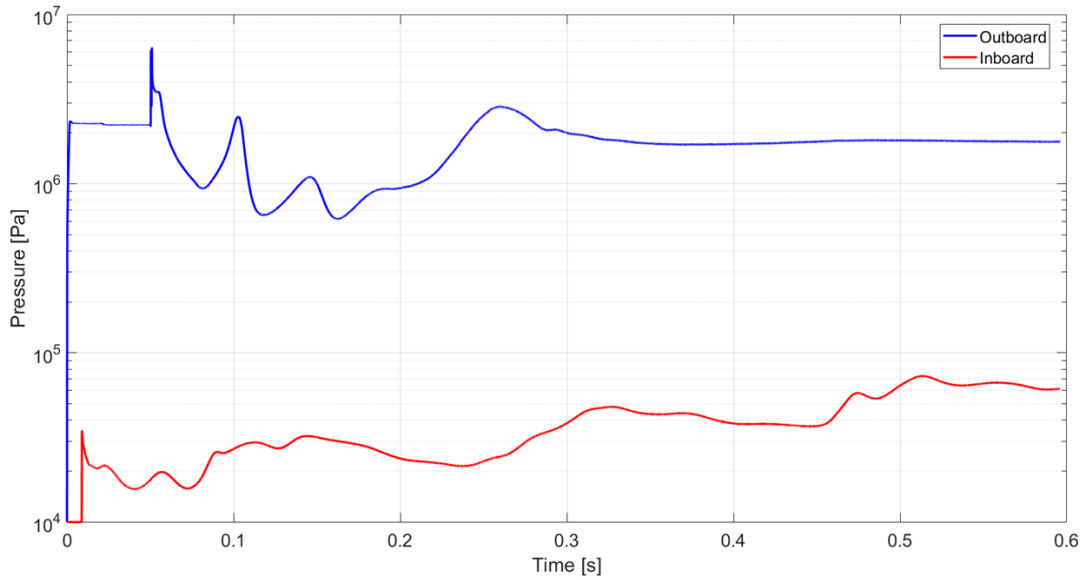

Figure 4.13: Pressure evolution in correspondence of "Outboard" point (represented by the blue line) and "Inboard" point (represented by the red line).

$\sim$ 2.00 m back to the pipe inlet. Note also how the profile at 55.0 ms doesn't present any peak, since the reflected wave has already impacted the outboard wall.

To provide a clearer insight of the phenomenon, a scalar scene of the volume fraction of water is developed for different time instants. The results are presented in figure 4.15, where the domain is limited to the area highlighted in green in figure 4.12 for a better visualization.

As the reflected wave approaches the inlet region, the Mach disk starts to be compressed and the "Outboard" point feels a pressure increase of approximately 44 bar, which can be observed in figure 4.13.
Proceeding with the transient, the Mach disk is completely dissipated, as stated in section 4.3.1, allowing the wave to reach the outboard wall, where the pressure raises almost instantly from $\sim$ 6 bar to $\sim$ 63 bar. The effects of this pressure spike on the wall should be carefully evaluated with a detailed structural analysis, which is however beyond the scope of this work. It is very interesting to notice that the pressure behaviour induced by the shock wave is consistent with that observed during a water hammer event in a fission reactor [41]. Moreover, the Joukowski equation can be used to evaluate the pressure increase induced by the wave, since it is valid also for two-phase mixtures [42]:

$$\Delta p = K \rho c_s \Delta v \tag{4.6}$$

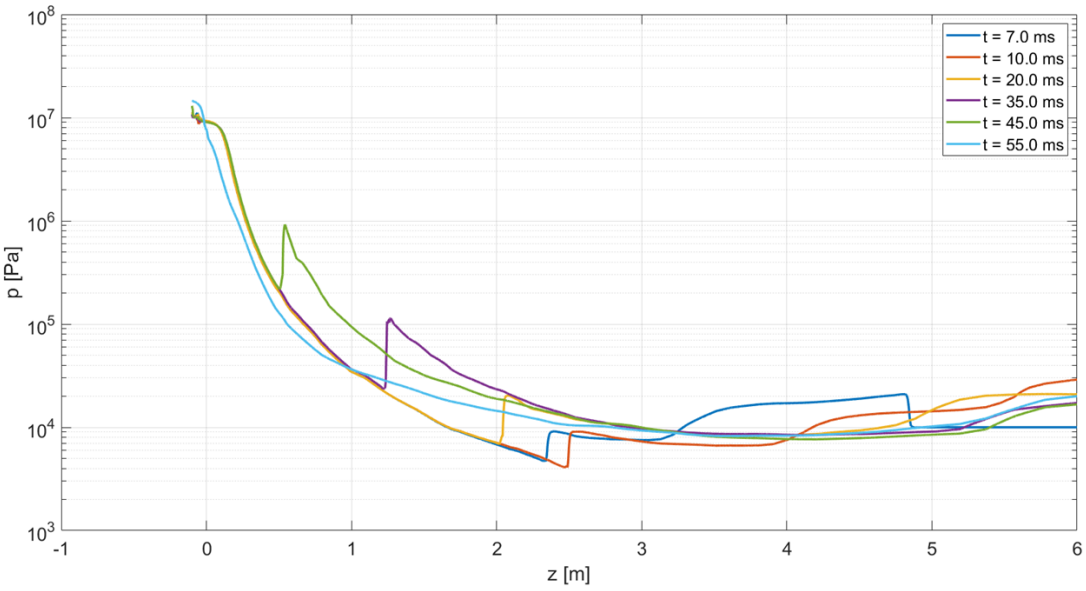

Figure 4.14: Pressure profile along the symmetry axis at different time instants; z represents the coordinate along the axis.

where Δp is the pressure difference across the discontinuity; K is a dimensionless coefficient which accounts for the nature of the blockage. In case of solid blockage it is equal to 1, while for liquid blockage it is equal to 0.5; ρ is the fluid density, which, for the case under exam, is taken equal to the vapor density; c_s is the speed of sound and Δv is the velocity difference across the discontinuity. As a result of applying equation 4.6 to the discontinuities presented in figure 4.14, a level of agreement within 30% is found. This means that there are indeed several similarities between the two events and therefore the wave-induced peaks are physically meaningful. In table 4.2 are presented the calculations carried out for three of the profiles shown in figure 4.14, respectively for t=20.0 ms t=35.0 ms and t=45.0 ms. Moreover, consistently with a water hammer event, the inlet mass flow rate shows a significant reduction when the wave impacts the inlet, as can be seen in figure 4.16.

It is worth highlighting that, when the reflected wave reaches the region near the inlet, the volume fraction of water in correspondence of the "Outboard" point shows a very rapid increase (see figure 4.17), hinting that the wave front is undergoing condensation.

The main effect of this vapor to water transition is to rapidly increase the density, leading to a much stronger compression and therefore to higher pressure peaks with respect to those observed in the analysis of a single-phase helium jet [22] (a rigorous comparison between the two transients is performed in section

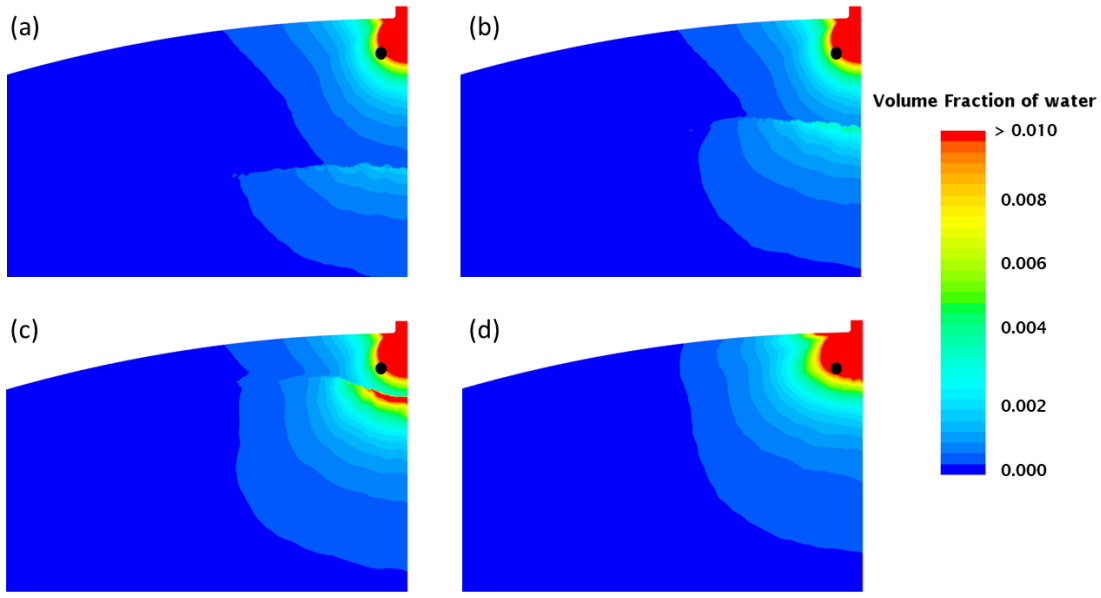

Figure 4.15: Volume fraction of water at (a) 35.0 ms, (b) 40.0 ms, (c) 45.0 ms and (d) 50.0 ms. The black dot superimposed on the scalar map represents the "Outboard" point

Table 4.2: Pressure jumps evaluated with the Joukowski equation.

t [ms]	K [-]	ρ_{vap} [kg/m^3]	c_s [m/s]	Δv [m/s]	Δp_{Jouk} [bar]	Δp_{CFD} [bar]	%ϵ [-]
20	0.5	0.10	523	544	0.1423	0.1450	1.9
35	0.5	0.50	525	575	0.7547	0.8229	8.3
45	0.5	4.40	535	483	5.6849	7.0000	18.8

4.4). It is also interesting to notice that the local peaks in the pressure profiles reported in figure 4.14 become progressively bigger, which means that the pressure difference across the discontinuities will also increase as the wave travels towards the inlet. The reason behind this behaviour is the following: if we look at the T-v water diagram (where $v = \frac{1}{\rho}$), reported in figure 4.18, we can see how for the same change in density, the pressure jump will be larger or smaller depending on the initial pressure of the fluid. In particular the higher is the initial pressure, the higher will be the pressure jump. This is consistent with what observed in the case under exam, as the density of the shock front increases rapidly, leading to higher

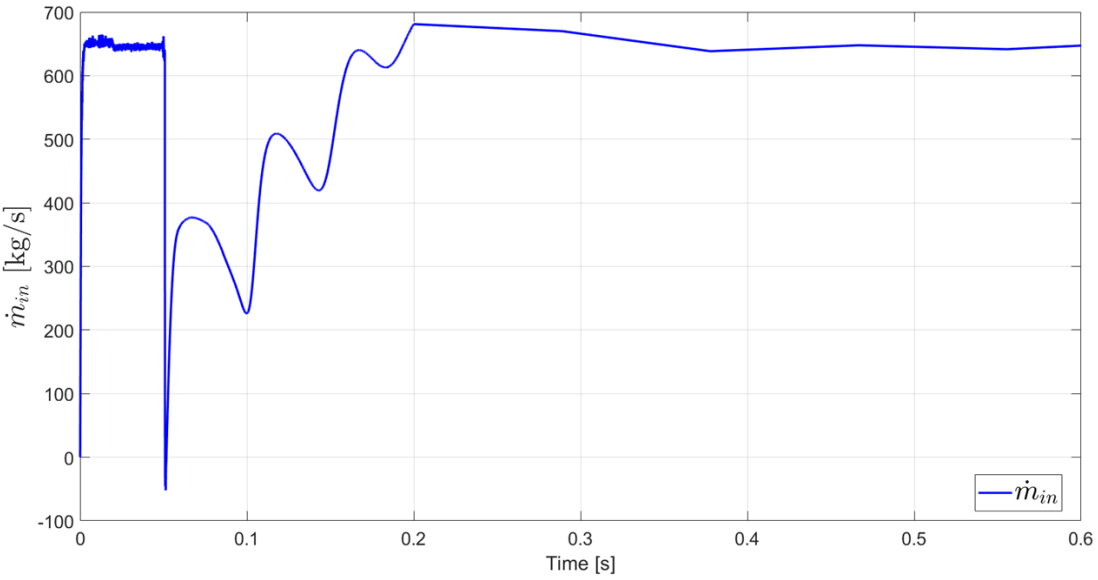

Figure 4.16: Inlet mass flow rate evolution.

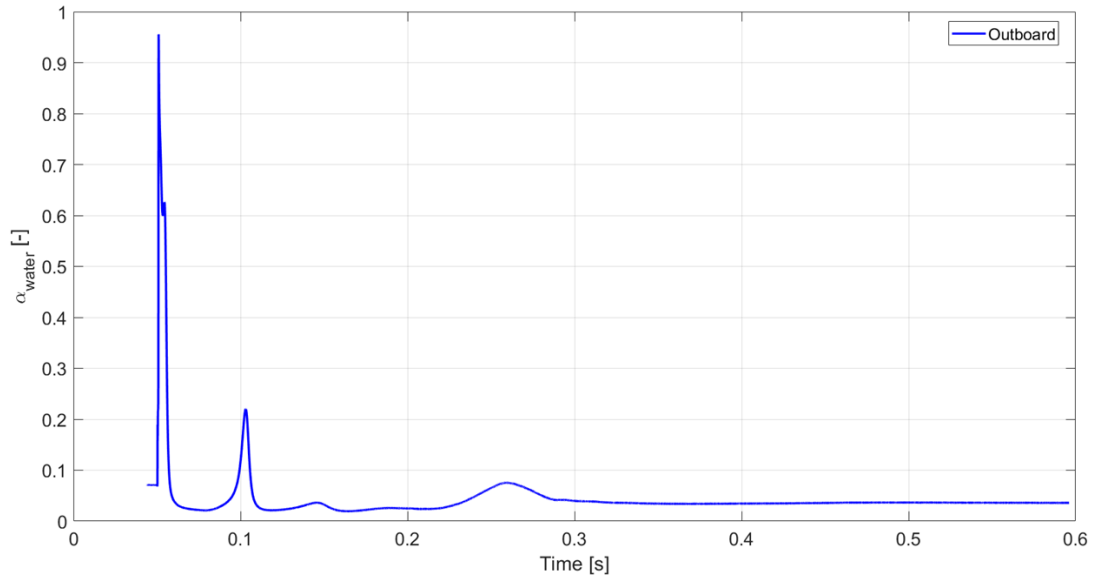

Figure 4.17: Volume fraction of water in correspondence with "outboard" point.

and higher pressure jumps.

The characteristic features of the phenomenon under exam recall those of the

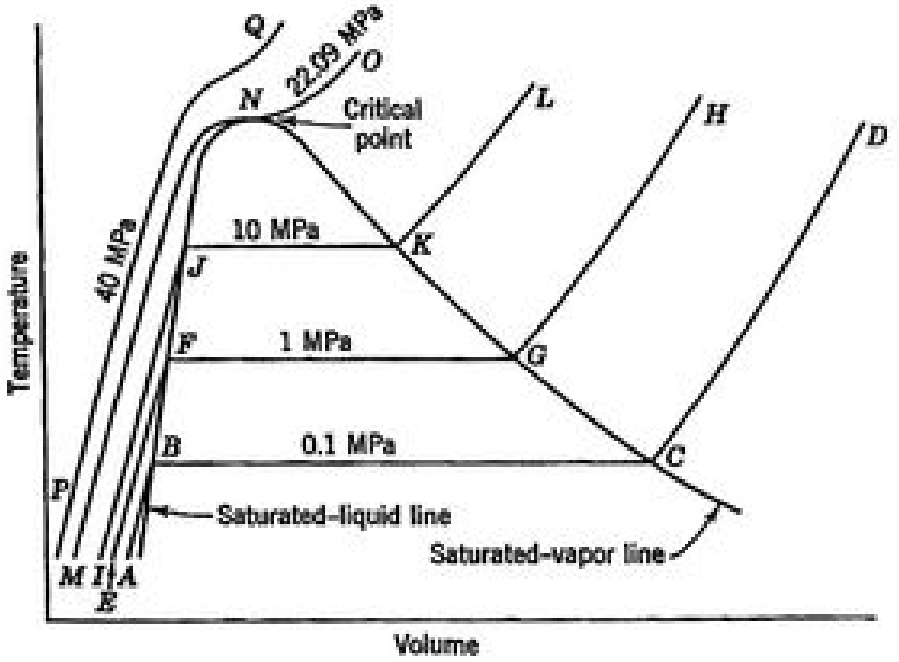

Figure 4.18: Water T-v diagram [43].

so-called Condensation-Induced Water Hammer (CIWH) event. The CIWH is a phenomenon typically occurring in nuclear fission reactors and it mainly involves the piping of emergency core cooling system and residual heat removal system. During the steam-water contact, a slug-flow is generated (see figure 4.19), which gives rise to low-pressure regions and accelerates the water streams [44]. There are four main CIWH occurrence mechanisms:

1. Steam-water counter-flow in a horizontal pipe
2. Sub-cooled water with condensing steam in a vertical pipe
3. Pressurized water entering a vertical steam-filled pipe
4. Hot water entering a lower pressure line

Even though this phenomenon is a concern if a single-phase liquid flows inside a pipe that contains saturated vapor, some of its features are also present in the case at hand: the pressure wave front is indeed characterized by high pressure and high fraction of liquid, and it comes into contact with vapor at low-pressure. Moreover,

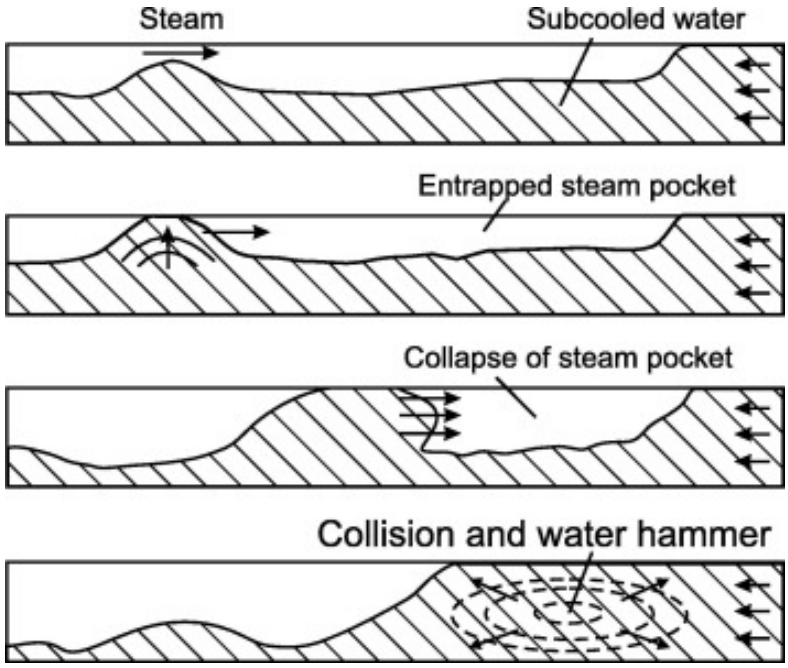

Figure 4.19: CIWH mechanism [45].

as observed in [45, 46, 47] the first pressure peak is the highest and it is followed by progressively smaller peaks, similarly to what observed in the case under exam (see figure 4.13). The main difference with respect to the problem at hand is the amplitude of the pressure peaks, which, in case of internal flows are much bigger, as can be seen in figure 4.20. This is because the flow, here, is not confined by a pipe and there is no closing valve, however, the presence of the inboard wall leads to similar consequences.

When the reflected waves are dissipated, the mass flow rate returns to its initial value and a second jet is generated, which however, as already discussed in section 4.3.1, is less energetic than the first one due to the increase in the average pressure. For this reason, the jet does not generate other reflected waves and assumes the typical shape of steady-state jets (see figure 4.11f).

In order to determine the end of the transient, it is necessary to monitor the pressure evolution on the BDs surface, because, as already discussed in section 4.1, they will open automatically when the pressure on their surface reaches 1.5 bar, allowing the VV to communicate with the VVPSS. The wave reaches the BDs after $\sim$ 68 ms, causing the pressure on their surface to increase from 0.1 bar to 0.5 bar. The main reason for this "weak" impact is that before reaching the region in which the BDs are located, the wave must travel throughout the whole torus, dissipating a lot of its energy. As shown in figure 4.21, after the pressure spike,

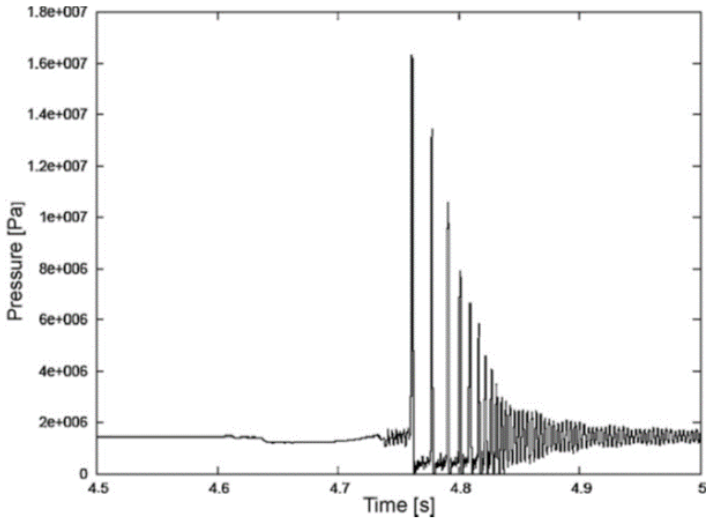

Figure 4.20: Pressure peaks in internal flow CIWH [46].

the BDs pressure starts increasing, following, in broad terms, the average pressure inside the VV for $\sim 2\,\mathrm{s}$ (i.e. when p_{avg} reaches $1.5\,\mathrm{bar}$).

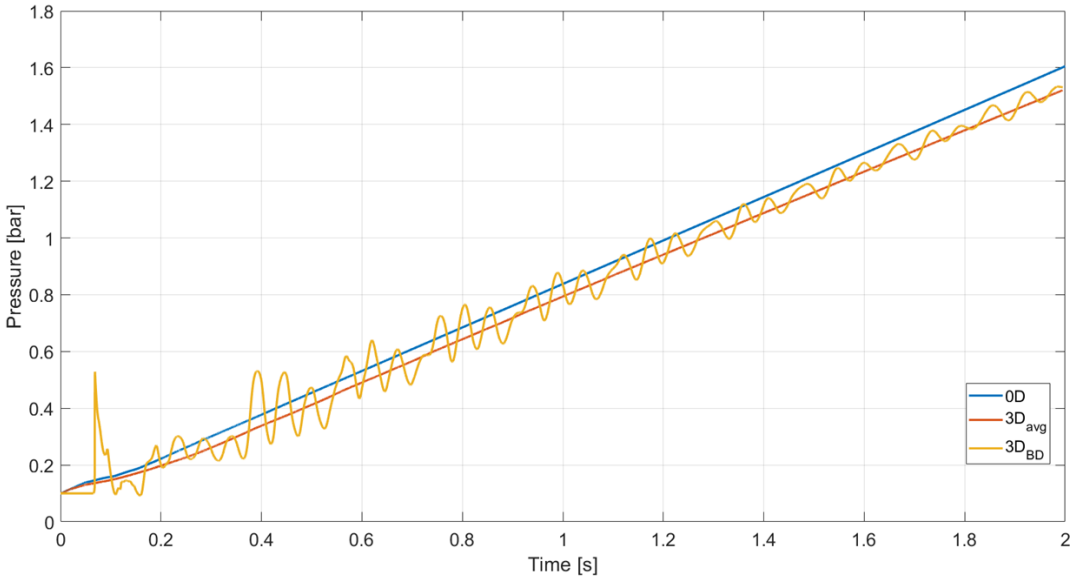

Figure 4.21: Average pressure inside the VV as computed by 3D CFD (red line) and 0D system-level code (blue line). The yellow line represents the BDs pressure evolution evaluated with CFD.

The analysis performed with a 0D tool, shows that as far as the pressurization time scale is concerned, a system-level model can be employed, as it gives conservative results (the blue line is always above the red line) and it requires much less computational effort with respect to a 3D CFD analysis.

4.3.3 Temperature Field

Figure 4.22 shows the temperature distribution at different time instants. It can be seen how the temperature inside the pipe is very high and it remains almost constant during the whole transient. On the contrary, right after the inlet area a rapid temperature decrease is experienced, down to a minimum value in correspondence of the discontinuity between the Mach disk and the leading edge (which is also the point where the velocity has the highest value). This point is called Minimum Temperature Distance (MTD) and, according to [27], it is an important parameter defining the end of the boiling and nucleation process inside a flashing jet. Moreover, beyond this point, the temperature should rise to reach the ambient one. Indeed, figure 4.22 shows that, moving downward, the temperature has a first, very rapid, increase and then decreases again to reach the wall value.

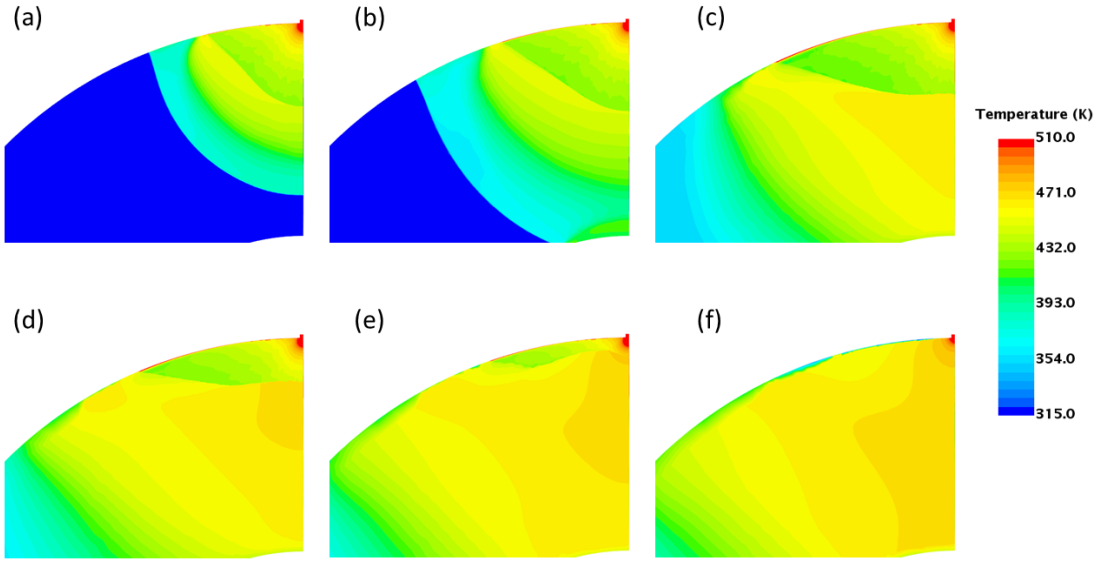

Figure 4.22: Temperature field at (a) 7.0 ms, (b) 10.0 ms, (c) 20.0 ms, (d) 35.0 ms, (e) 45.0 ms and (f) 55.0 ms.

The axial temperature profile at different time instants is shown in figure 4.23. First of all, a global increase of temperature can be noticed going from 7.0 ms to 55.0 ms. Then, consistently with what observed in the pressure profile in section 4.3.2, also in this case is possible to see how the peak shifts from the blue line to the red one before the impact and from the yellow line back to the cyan one right after (i.e. the shock wave hits the front wall and it is reflected back).

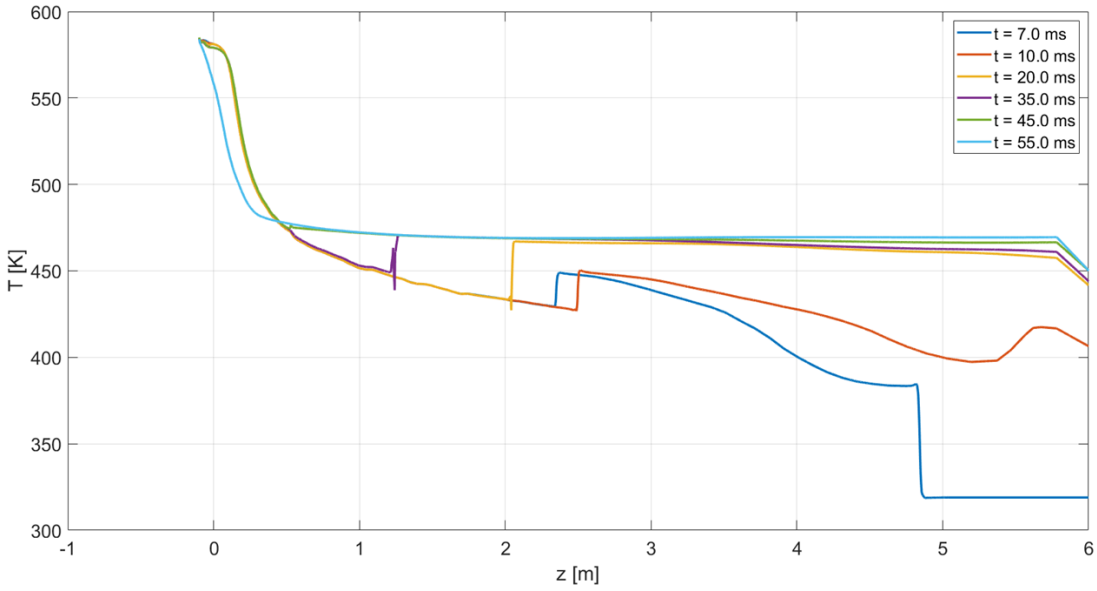

Figure 4.23: Temperature profile along the symmetry axis at different time instants; z represents the coordinate along the axis.

4.4 Comparison with the Helium-Cooled Breeding Blanket

The two main BB concepts which are currently being studied for the EU DEMO reactor are the WCLL [7, 8] and the HCPB [6]. Similarly to what has been done in this work, a CFD analysis of an in-VV LOCA originating by a failure in a helium-cooled blanket, has been carried out by Zappatore et al. in [22]. In this section the main differences between the two transients are highlighted with the aim of establishing which one leads to the most severe consequences. The first difference is of course the employed coolant, as the current design of the HCPB foresees the use of pressurized helium at 80 bar and 300 °C÷520 °C. Another major difference with respect to the water case, is that the helium remain gaseous for the whole transient, giving rise to a hypersonic single-phase jet, which is not affected by the phase-change mechanisms. The higher velocity allows the jet to develop mainly along the axial direction (see figure 4.24) and, therefore, to dissipate much less energy with respect to the water jet. The latter, on the contrary, expands in all directions, as the vapor enters at a significantly lower speed due to the flashing phenomenon occurring at the pipe exit. Indeed, in the case of helium, the leading edge reaches the front wall in less than 2.5 ms, against the 9.5 ms of the water case. Also the impact with the wall is quite different: the helium jet, being much more energetic, causes the pressure to increase from 0.1 bar to 3.5 bar, while, in the case of water, the pressure rises up to 0.35 bar.

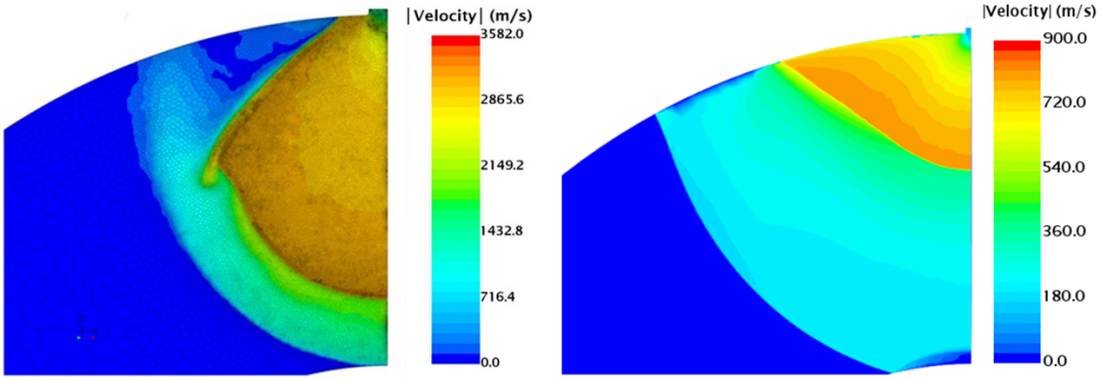

Figure 4.24: Comparison between the helium jet [22] (left) and the water jet (right) velocity field at the moment of the impact with the front wall.

Following the impact with the front wall, a reflected wave is generated, which

is much stronger for the water case, as the wave front undergoes condensation. The result of this phase change mechanism is that the wave has enough energy to completely dissipate the Mach disk and to reach the inlet. As a consequence, the inlet mass flow rate is strongly reduced and the outboard wall experiences a pressure increase of approximately 57 bar. On the contrary, the wave generated in the helium transient, is not energetic enough to compress the Mack disk (which is much bigger and stronger than that of water) and therefore it doesn't reach the outboard wall.

Concerning the temperature field, the two transients present a similar behaviour, with an almost constant temperature distribution inside the pipe, followed by a rapid decrease along the Mack disk and a successive increase to reach the ambient value. However, the maximum and minimum temperatures reached are very different: the helium jet is characterized by both very high ($\sim$ 1,500 K) and very low ($\sim$ 30 K) temperatures, while for the water jet, as can be noticed in section 4.3.3, the temperature is always between 290 K and 600 K.

The timescales involved in the two transients are also very different. In particular, during the helium transient, the leading shock reaches the BDs in less than 20 ms, causing the pressure on their surface to increase up to 2.5 bar almost immediately. Furthermore, the average pressure inside the VV increase more rapidly, reaching the 1.5 bar threshold for the opening of the BDs, in just 53 ms. The water transient is instead slower and less violent due to the different expansion mechanism that characterizes the flashing jet. The leading edge reaches the BDs after 68 ms, but in this case the impact with the wall is relatively weak, as the pressure on the BDs surface goes from 0.1 bar to 0.5 bar only. In addition, the average pressure in the chamber takes 2 s to reach the BDs opening threshold, therefore the communication between the VV and the VVPSS will occur much later with respect to the helium transient.

Chapter 5

Conclusions

A 3D CFD model of an in-VV LOCA originating from a break in the WCLL-BB of the EU DEMO reactor has been developed. The main objective was to simulate the evolution of the two-phase flashing jet inside the vacuum chamber and its effects on the structural integrity of the reactor walls. The model is able to capture the different shock waves generated when the pressurized water enters the plasma chamber, as well as the local pressure peaks on the tokamak walls. In particular, thanks to the employed adaption refinement algorithm, the adopted mesh is able to progressively adapt to the solution during the transient, minimizing the number of cells and therefore the computational effort. The model was first benchmarked against a simpler 2D problem taken from the literature, which presents similar characteristics and then applied to the EU DEMO relevant case. In particular, this approach allowed to test the most relevant features of the simulation such as the multiphase approach or the turbulence model. The results show that the pressure peak caused by the impact of the shock front with the inboard wall, is below the design limits and therefore doesn't represent a problem for the structural integrity of the chamber. On the contrary, the reflected wave generated right after, undergoes a condensation process while moving back to the inlet region, becoming more energetic and causing a relatively strong impact with the outboard wall, whose effects should be assessed with a detailed mechanical analysis.
Moving on with the transient, the pressure wave reaches the opposite side of the torus, where the safety burst disks are located, and impacts on their surface. According to the results, the pressure peak is not of concern, since the wave loses a lot of energy before reaching that point. Moreover, the evolution of the BDs pressure starts following that of the average pressure inside the vessel until the end of the simulation (i.e. after 2 s from the occurrence of the break), when it reaches 1.5 bar and causes the burst disk to automatically open. The comparison with a 0D model , shows that a 0D analysis is sufficient to predict the average pressure behaviour during the transient and therefore the opening time of the burst disks.

On the contrary, the local parameters such as the pressure peaks on the reactor walls, can be evaluated only by means of detailed 3D CFD.
Finally, a comparison with an in-VV LOCA originating from a break in the helium-cooled BB has been carried out. It turned out that the helium transient is much stronger than that of water and also the velocities involved are much higher. Indeed, not being subjected to phase change mechanisms, the helium jet is able to reach hypersonic velocities and to dissipate much less energy, causing steeper pressure peaks on the chamber walls.
Further development of the model may include a more complex geometry, which accounts for all the 262 cooling channels and doesn't neglect the divertor region. Moreover, the very first instants after the pipe break could be modeled with different tools in order to cover the time interval needed for the pressure to rise from 1 Pa-10 Pa to 10,000 Pa (0.1 bar).

Bibliography

[1] David Moiraf. «The use of Plasma Mirror for Relativistic Electron Generation Relevant to Fast Ignition in Inertial Confinement Fusion». PhD thesis. July 2020 (cit. on p. 2).

[2] URL: https://euro-fusion.org/ (cit. on p. 3).

[3] Philippe Magaud, G. Marbach, and Ian J. Cook. «Nuclear Fusion Reactors». In: 2004 (cit. on p. 3).

[4] Curt Gliss. *DEMO reference configuration model*. EFDA_D_2MUNPL. EUROfusion Consortium, 2017 (cit. on p. 4).

[5] G. Federici, L. Boccaccini, F. Cismondi, M. Gasparotto, Y. Poitevin, and I. Ricapito. «An overview of the EU breeding blanket design strategy as an integral part of the DEMO design effort». In: *Fusion Engineering and Design* 141 (2019), pp. 30–42. ISSN: 0920-3796. DOI: https://doi.org/10.1016/j.fusengdes.2019.01.141. URL: https://www.sciencedirect.com/science/article/pii/S0920379619301590 (cit. on p. 3).

[6] Francisco A. Hernández et al. «Consolidated design of the HCPB Breeding Blanket for the pre-Conceptual Design Phase of the EU DEMO and harmonization with the ITER HCPB TBM program». In: *Fusion Engineering and Design* 157 (2020), p. 111614. ISSN: 0920-3796. DOI: https://doi.org/10.1016/j.fusengdes.2020.111614. URL: https://www.sciencedirect.com/science/article/pii/S0920379620301629 (cit. on pp. 3, 55).

[7] G.A. Spagnuolo et al. «Integrated design of breeding blanket and ancillary systems related to the use of helium or water as a coolant and impact on the overall plant design». In: *Fusion Engineering and Design* 173 (2021), p. 112933. ISSN: 0920-3796. DOI: https://doi.org/10.1016/j.fusengdes.2021.112933. URL: https://www.sciencedirect.com/science/article/pii/S0920379621007092 (cit. on pp. 3, 35, 55).

[8] L.V. Boccaccini et al. «Status of maturation of critical technologies and systems design: Breeding blanket». In: *Fusion Engineering and Design* 179 (2022), p. 113116. ISSN: 0920-3796. DOI: https://doi.org/10.1016/j.fusengdes.2022.113116. URL: https://www.sciencedirect.com/science/article/pii/S0920379622001168 (cit. on pp. 3, 55).

[9] J. Aubert et al. «Design and preliminary analyses of the new Water Cooled Lithium Lead TBM for ITER». In: *Fusion Engineering and Design* 160 (2020), p. 111921. ISSN: 0920-3796. DOI: https://doi.org/10.1016/j.fusengdes.2020.111921. URL: https://www.sciencedirect.com/science/article/pii/S0920379620304695 (cit. on p. 5).

[10] Alessandro Del Nevo et al. «WCLL breeding blanket design and integration for DEMO 2015: Status and perspectives». In: *Fusion Engineering and Design* 124 (Mar. 2017). DOI: 10.1016/j.fusengdes.2017.03.020 (cit. on p. 5).

[11] A. Froio. *Slides of the master course "Nuclear Fusion Reactor Enegineering"*. Politecnico di Torino. 2022 (cit. on p. 5).

[12] Matteo D'Onorio, Fabio Giannetti, Maria Teresa Porfiri, and Gianfranco Caruso. «Preliminary safety analysis of an in-vessel LOCA for the EU-DEMO WCLL blanket concept». In: *Fusion Engineering and Design* 155 (2020), p. 111560. ISSN: 0920-3796. DOI: https://doi.org/10.1016/j.fusengdes.2020.111560. URL: https://www.sciencedirect.com/science/article/pii/S0920379620301083 (cit. on p. 7).

[13] Mu-Young Ahn, Seungyon Cho, Duck Hoi Kim, Eun-Seok Lee, Hyung-Seok Kim, Jae-Seung Suh, Sunghwan Yun, and Nam Zin Cho. «Preliminary safety analysis of Korea Helium Cooled Solid Breeder Test Blanket Module». In: *Fusion Engineering and Design* 83.10 (2008). Proceedings of the Eight International Symposium of Fusion Nuclear Technology, pp. 1753–1758. ISSN: 0920-3796. DOI: https://doi.org/10.1016/j.fusengdes.2008.06.059. URL: https://www.sciencedirect.com/science/article/pii/S0920379608001944 (cit. on p. 7).

[14] Antonio Froio, Andrea Bertinetti, Sergio Ciattaglia, Fabio Cismondi, Laura Savoldi, and Roberto Zanino. «Modelling an in-vessel loss of coolant accident in the EU DEMO WCLL breeding blanket with the GETTHEM code». In: *Fusion Engineering and Design* 136 (2018), pp. 1226–1230. DOI: 10.1016/j.fusengdes.2018.04.106 (cit. on p. 7).

[15] Antonio Froio, Luciana Barucca, Sergio Ciattaglia, Fabio Cismondi, Laura Savoldi, and Roberto Zanino. «Analysis of the effects of primary heat transfer system isolation valves in case of in-vessel loss-of-coolant accidents in the EU DEMO». In: *Fusion Engineering and Design* 159 (2020), p. 111926. DOI: 10.1016/j.fusengdes.2020.111926 (cit. on p. 7).

[16] M. Nakamura, K. Tobita, Y. Someya, H. Utoh, Y. Sakamoto, and W. Gulden. «Thermohydraulic responses of a water-cooled tokamak fusion DEMO to loss-of-coolant accidents». In: *Nuclear Fusion* 55.12 (Oct. 2015), p. 123008. DOI: 10.1088/0029-5515/55/12/123008. URL: https://dx.doi.org/10.1088/0029-5515/55/12/123008 (cit. on pp. 7, 37).

[17] B.R. Munson, A.P. Rothmayer, and T.H. Okiishi. *Fundamentals of Fluid Mechanics, 7th Edition*. Blackwell handbooks in linguistics. Wiley, 2012. ISBN: 9781118214596. URL: https://books.google.it/books?id=GQMcAAAAQBAJ (cit. on p. 8).

[18] Erwin Franquet, Vincent Perrier, Stéphane Gibout, and Pascal Bruel. «Free underexpanded jets in a quiescent medium: A review». In: *Progress in Aerospace Sciences* 77 (2015), pp. 25–53. ISSN: 0376-0421. DOI: https://doi.org/10.1016/j.paerosci.2015.06.006. URL: https://www.sciencedirect.com/science/article/pii/S0376042115000548 (cit. on pp. 8, 43).

[19] R.D. Zucker and O. Biblarz. *Fundamentals of Gas Dynamics*. Wiley, 2019. ISBN: 9781119481706. URL: https://books.google.it/books?id=kreuDwAAQBAJ (cit. on p. 8).

[20] A. H. Shapiro. *The Dynamics and Thermodynamics of Compressible Fluid Flow*. Vol. 1. New York: Wiley, 1953 (cit. on p. 8).

[21] URL: https://aerospaceweb.org/question/propulsion/q0224.shtml (cit. on p. 9).

[22] Andrea Zappatore, Antonio Froio, Gandolfo Alessandro Spagnuolo, and Roberto Zanino. «3D transient CFD simulation of an in-vessel loss-of-coolant accident in the EU DEMO fusion reactor». In: *Nuclear Fusion* 60.12 (Sept. 2020), p. 126001. DOI: 10.1088/1741-4326/abac6b. URL: https://dx.doi.org/10.1088/1741-4326/abac6b (cit. on pp. 9, 41, 43, 47, 55).

[23] MATEI I. RADULESCU and CHUNG K. LAW. «The transient start of supersonic jets». In: *Journal of Fluid Mechanics* 578 (2007), pp. 331–369. DOI: 10.1017/S0022112007004715 (cit. on p. 8).

[24] R. ISHII, H. FUJIMOTO, N. HATTA, and Y. UMEDA. «Experimental and numerical analysis of circular pulse jets». In: *Journal of Fluid Mechanics* 392 (1999), pp. 129–153. DOI: 10.1017/S0022112099005303 (cit. on p. 8).

[25] Yixiang Liao and Dirk Lucas. «Computational modelling of flash boiling flows: A literature survey». In: *International Journal of Heat and Mass Transfer* 111 (Aug. 2017), pp. 246–265. DOI: 10.1016/j.ijheatmasstransfer.2017.03.121 (cit. on p. 10).

[26] H.W.M. Witlox, P.J. Bowen, Great Britain. Health, Safety Executive, and Det Norske Veritas Ltd. *Flashing Liquid Jets and Two-phase Dispersion: A Review*. HSE contract research report. HSE Books, 2001. ISBN: 9780717622504. URL: https://books.google.it/books?id=9rraAAAACAAJ (cit. on p. 10).

[27] Geanette Polanco, Arne Erik Holdø, and George Munday. «General review of flashing jet studies». In: *Journal of Hazardous Materials* 173.1 (2010), pp. 2–18. ISSN: 0304-3894. DOI: https://doi.org/10.1016/j.jhazmat.2009.08.138. URL: https://www.sciencedirect.com/science/article/pii/S0304389409013090 (cit. on pp. 10, 53).

[28] Hengjie Guo, Lorenzo Nocivelli, Roberto Torelli, and Sibendu Som. «Towards understanding the development and characteristics of under-expanded flash boiling jets». In: *International Journal of Multiphase Flow* 129 (2020), p. 103315. ISSN: 0301-9322. DOI: https://doi.org/10.1016/j.ijmultiphaseflow.2020.103315. URL: https://www.sciencedirect.com/science/article/pii/S0301932219309693 (cit. on p. 10).

[29] Siemens Digital Industries Software. *Simcenter STAR-CCM+ User Guide v. 2021.2*. Version 2021.2. Siemens 2021 (cit. on pp. 14–16, 18, 25, 26).

[30] Martin Sommerfeld. «Numerical Methods for Dispersed Multiphase Flows». In: July 2017, pp. 327–396. ISBN: 978-3-319-60281-3. DOI: 10.1007/978-3-319-60282-0_6 (cit. on p. 17).

[31] Yixiang Liao and Dirk Lucas. «Computational modelling of flash boiling flows: A literature survey». In: *International Journal of Heat and Mass Transfer* 111 (Aug. 2017), pp. 246–265. DOI: 10.1016/j.ijheatmasstransfer.2017.03.121 (cit. on p. 18).

[32] M. De Lorenzo, Ph. Lafon, M. Di Matteo, M. Pelanti, J.-M. Seynhaeve, and Y. Bartosiewicz. «Homogeneous two-phase flow models and accurate steam-water table look-up method for fast transient simulations». In: *International Journal of Multiphase Flow* 95 (2017), pp. 199–219. ISSN: 0301-9322. DOI: https://doi.org/10.1016/j.ijmultiphaseflow.2017.06.001. URL: https://www.sciencedirect.com/science/article/pii/S0301932216307236 (cit. on pp. 18, 19).

[33] Akihiko MINATO, Kazuhide TAKAMORI, and Akira SUSUKI. «Numerical Study of Two-Dimensional Structure in Critical Steam-Water Two-Phase Flow». In: *Journal of Nuclear Science and Technology* 32.5 (1995), pp. 464–475. DOI: 10.1080/18811248.1995.9731732. eprint: https://doi.org/10.1080/18811248.1995.9731732. URL: https://doi.org/10.1080/18811248.1995.9731732 (cit. on pp. 21–23, 26–31).

[34] Matteo D'Onorio, Tommaso Glingler, Guido Mazzini, Maria Teresa Porfiri, and Gianfranco Caruso. «Passive Hydrogen Recombination during a Beyond Design Basis Accident in a Fusion DEMO Plant». In: *Energies* 16.6 (2023). ISSN: 1996-1073. DOI: 10.3390/en16062569. URL: https://www.mdpi.com/1996-1073/16/6/2569 (cit. on p. 33).

[35] Antonio Froio. «Number of channels involved following a break in the EU DEMO HCPB and WCLL BB FW». Version 1.0.0. In: (July 2020). DOI: 10.5281/zenodo.3937295. URL: https://doi.org/10.5281/zenodo.3937295 (cit. on p. 35).

[36] Bastian E. Rapp. «Chapter 9 - Fluids». In: *Microfluidics: Modelling, Mechanics and Mathematics*. Ed. by Bastian E. Rapp. Micro and Nano Technologies. Oxford: Elsevier, 2017, pp. 243–263. ISBN: 978-1-4557-3141-1. DOI: https://doi.org/10.1016/B978-1-4557-3141-1.50009-5. URL: https://www.sciencedirect.com/science/article/pii/B9781455731411500095 (cit. on p. 36).

[37] G.A. Bird. *Molecular Gas Dynamics and the Direct Simulation of Gas Flows*. Molecular Gas Dynamics and the Direct Simulation of Gas Flows v. 1. Clarendon Press, 1994. ISBN: 9780198561958. URL: https://books.google.it/books?id=Bya5QgAACAAJ (cit. on p. 37).

[38] G.F. Nallo, G. Mazzitelli, L. Savoldi, F. Subba, and R. Zanino. «Self-consistent modelling of a liquid metal box-type divertor with application to the divertor tokamak test facility: Li versus Sn». In: *Nuclear Fusion* 59.6 (May 2019), p. 066020. DOI: 10.1088/1741-4326/ab145b. URL: https://dx.doi.org/10.1088/1741-4326/ab145b (cit. on p. 37).

[39] Xue Zhou Jin. «BB LOCA analysis for the reference design of the EU DEMO HCPB blanket concept». In: *Fusion Engineering and Design* 136 (2018). Special Issue: Proceedings of the 13th International Symposium on Fusion Nuclear Technology (ISFNT-13), pp. 958–963. ISSN: 0920-3796. DOI: https://doi.org/10.1016/j.fusengdes.2018.04.046. URL: https://www.sciencedirect.com/science/article/pii/S092037961830334X (cit. on p. 37).

[40] Antonio Froio, Andrea Bertinetti, Laura Savoldi, R Zanino, F Cismondi, and Sergio Ciattaglia. «Benchmark of the GETTHEM Vacuum Vessel Pressure Suppression System (VVPSS) model for a helium-cooled EU DEMO blanket». In: June 2017, pp. 11–11. ISBN: 9781315210469. DOI: 10.1201/9781315210469-9 (cit. on p. 37).

[41] Mohamed S. Ghidaoui, Ming Zhao, Duncan A. McInnis, and David H. Axworthy. «A Review of Water Hammer Theory and Practice ». In: *Applied Mechanics Reviews* 58.1 (Mar. 2005), pp. 49–76. ISSN: 0003-6900. DOI: 10.1115/1.1828050. eprint: https://asmedigitalcollection.asme.org/appliedmechanicsreviews/article-pdf/58/1/49/5440913/49_1.pdf. URL: https://doi.org/10.1115/1.1828050 (cit. on p. 46).

[42] P Griffith. *Screening reactor steam/water piping systems for water hammer*. Tech. rep. OSTI, Sept. 1997. DOI: 10.2172/527558. URL: https://www.osti.gov/biblio/527558 (cit. on p. 46).

[43] URL: https://web.mit.edu/16.unified/www/FALL/thermodynamics/notes/node61.html (cit. on p. 50).

[44] Lutao Wang, Xiaoyu Yue, Daotong Chong, Weixiong Chen, and Junjie Yan. «Experimental investigation on the phenomenon of steam condensation induced water hammer in a horizontal pipe». In: *Experimental Thermal and Fluid Science* 91 (2018), pp. 451–458. ISSN: 0894-1777. DOI: https://doi.org/10.1016/j.expthermflusci.2017.10.036. URL: https://www.sciencedirect.com/science/article/pii/S0894177717303424 (cit. on p. 50).

[45] C. Urban and M. Schlüter. «Investigations on the stochastic nature of condensation induced water hammer». In: *International Journal of Multiphase Flow* 67 (2014), pp. 1–9. ISSN: 0301-9322. DOI: https://doi.org/10.1016/j.ijmultiphaseflow.2014.08.001. URL: https://www.sciencedirect.com/science/article/pii/S0301932214001402 (cit. on p. 51).

[46] Imre Ferenc Barna, Attila Rikárd Imre, Gábor Baranyai, and György Ézsöl. «Experimental and theoretical study of steam condensation induced water hammer phenomena». In: *Nuclear Engineering and Design* 240.1 (2010), pp. 146–150. ISSN: 0029-5493. DOI: https://doi.org/10.1016/j.nucengdes.2009.09.027. URL: https://www.sciencedirect.com/science/article/pii/S0029549309004853 (cit. on pp. 51, 52).

[47] *Numerical Simulation of Condensation Induced Water Hammer*. Vol. 12th International Conference on Nuclear Engineering, Volume 1. International Conference on Nuclear Engineering. Apr. 2004, pp. 791–795. DOI: 10.1115/ICONE12-49404. eprint: https://asmedigitalcollection.asme.org/ICONE/proceedings-pdf/ICONE12/46873/791/2614063/791_1.pdf. URL: https://doi.org/10.1115/ICONE12-49404 (cit. on p. 51).